XFEM to couple nonlocal micromechanics damage with discrete mode I cohesive fracture

Wencheng Jin[a], Chloé Arson[b],*

[a] *Energy and Environment Science & Technology Directorate, Idaho National Laboratory, USA*
[b] *School of Civil and Environmental Engineering, Georgia Institute of Technology, USA*

Highlights

- Proposed a novel framework that couples a nonlocal anisotropic damage model with a cohesive zone model to simulate the nucleation of micro-cracks towards the formation of a macro-fracture.
- Established the transition criteria from diffused damage to localized fracture based on a critical damage threshold; the threshold is determined by considering micro-crack interaction.
- Implemented an XFEM algorithm that ensures that the energy dissipated at the macro level by propagating the fracture is equal to that dissipated at the micro-level by propagating damage before the transition to fracture.

Abstract

   A computational tool is developed to simulate the propagation of a discrete fracture within a continuum damage process zone. Microcrack initiation and propagation prior to coalescence are represented by a nonlocal anisotropic Continuum Damage Mechanics (CDM) model in which the crack density is calculated explicitly. A damage threshold is defined to mark the beginning of crack coalescence. When that threshold is reached, a cohesive segment is inserted in the mesh to replace a portion of the damage process zone by a segment of discrete fracture. Discretization is done with the extended Finite Element Method (XFEM), which makes it possible to simulate fracture propagation without assigning the fracture path *a priori*. Rigorous calibration procedures are established for the cohesive strength (related to the damage threshold) and for the cohesive energy release rate, to ensure the balance of energy dissipated at the micro and macro scales. The XFEM-based tool is implemented into an open source object-oriented numerical package (OOFEM), and used to simulate wedge splitting and three-point bending tests. Results demonstrate that the proposed numerical method captures the entire failure process in mode I, from a mesh-independent diffuse damage zone to a localized fracture. Future work will investigate mixed mode fracture propagation.
ⓒ 2019 Elsevier B.V. All rights reserved.

---

* Corresponding author.
   E-mail address: chloe.arson@ce.gatech.edu (C. Arson).

1. Introduction

Macro-fracture propagation results from micro-crack coalescence. Modeling fracture propagation at the macro-scale in interaction with micro-scale structure evolution is of great interest in many fields of engineering. Over the last few decades, numerous numerical methods were proposed to model multiscale fracture propagation, including: (1) Direct numerical simulation (brute-force full scale simulation); (2) Homogenization-based multiscale approach; and (3) Damage–fracture transition techniques.

In direct numerical simulation approaches, the morphology of each microstructure phase (grains, voids, micro-cracks) is explicitly discretized and each phase is assigned its specific constitutive model. For example, Brazilian tests of rock materials [1] were simulated directly with the discrete element method (DEM) and three-point bending tests of asphalt concrete [2] were simulated directly with the finite element method (FEM). Direct numerical simulations only require the micromechanical behavior, through constitutive laws in FEM and contact bonds in DEM. The macroscopic behavior is represented by the superposition of microscopic behaviors. Direct numerical simulations are very efficient to predict fracture initiation and propagation at laboratory scale. However, the computational cost is not manageable for metric-scale problems, even with state-of-the-art supercomputing capabilities.

The computational homogenized multiscale simulation method can be used in replacement of the standard stress–strain phenomenological constitutive models that depend on macroscopic internal variables. The pointwise overall stress–strain behavior (i.e. stress–strain behavior at each Gauss point), evaluated from the solution of an auxiliary Boundary Value Problem (BVP) over a Representative Elementary Volume (REV), is endowed with a geometrical description of the material morphology [3]. Computation Homogenization (CH) is used to connect the two scales. Several CH techniques exist [4]. In the standard CH, the macroscopic kinematic quantities (strain or deformation gradient) are downscaled to the micro-scale as boundary conditions to solve the BVP. Once the micro-scale BVP with explicit inhomogeneities is solved by the FEM, CH is performed over the REV to obtain the stress tensor and the Jacobian at the macroscopic level. Because finite element simulations are performed to solve two nested BVPs (micro and macro), the method is also known as FE^2 scheme [5]. By contrast, continuous–discontinuous homogenization consists in incorporating a discrete crack at the macro-scale — a technique known as the multi-scale discontinuity aggregation method [6–8]. Aside from the continuous–discontinuous CH, efforts were made to homogenize the continuum softening behavior at the micro-scale into a cohesive zone model at the macro-scale [9–11]: the macro-scale interfacial displacement jump is downscaled as a boundary condition for a micro-scale interfacial REV with finite thickness, and the solution of interfacial REV traction is upscaled as the macro-scale cohesive traction by homogenization. Compared to the direct simulation method, CH schemes are efficient to simulate engineering problems at the metric scale. However, CH is still computationally expensive because of the hierarchical BVPs simulation. In addition, constitutive laws at micro-scale are still required and may not be known *a priori*.

The technique of transition from damage to fracture consists in coupling a Continuum Damage Mechanics (CDM) model with a discrete fracture mechanics model using an advanced discretization method. As explained in [12–16], the failure process of quasi-brittle materials involves two stages: diffused damage inception followed by extensive damage localization leading to macro-fracture propagation. In the following, we call "process zone" the zone with diffused micro crack inception in the first stage. The most widely used numerical tools to model the failure process are classified either as CDM methods or as fracture mechanics methods. CDM methods employ constitutive laws with full stress softening and regularization techniques [17–19] and allow capturing diffused damage arising at the early phase of material failure, in the form of stiffness degradation. However, it cannot explicitly predict the formation of macro fracture surfaces, and it suffers from spurious damage development due to excessive strain under high stress [20,21]. Fracture mechanics models can avoid the issues encountered in nonlocal CDM models by creating discrete surfaces. However, linear elastic fracture mechanics models cannot account for the development of the damage process zone. In the widely used Cohesive Zone Models (CZM), the process zone is lumped into a single line (respectively, a single surface) in 2D (respectively, 3D). Besides, the implementation of fracture mechanics models is challenging because the dynamic representation of discrete fracture surfaces requires sophisticated finite element discretization. The embedded crack method [12], the eXtended Finite Element Method (XFEM) [16], and the method of interface-element-inserted-on-the-fly [22] are among the most efficient techniques available to date to discretize the domain to conform with the geometry of the fracture. It is also worth noting that the phase-field method belongs to the category of continuum damage models. As demonstrated in [23–25], phase-field

fracture propagation models are numerically equivalent to an integration based nonlocal isotropic damage model, and are mathematically similar to gradient-based non-local damage models. Phase-field methods are computationally efficient but face serious challenges when it is required to model fracture surfaces explicitly.

Provided that neither CDM models nor fracture mechanics models alone can properly represent the two stages of fracture propagation, a coherent computational framework that models the transition from diffused damage to localized cohesive fracture is desirable. The very first attempt of coupling CDM and fracture mechanics was made by Planas and collaborators [26], who proved that the cohesive fracture model is a particular case of nonlocal damage formulation. Later, Mazars and Pijaudier–Cabot published a paper [27] in which they established an equivalence between the energy dissipated for opening a discrete fracture and the energy dissipated for producing a dilute distribution of micro-cracks (diffused damage). This energy equivalence was further used by Cazes and collaborators [28,29] to construct a cohesive law from a nonlocal damage model in the framework of thermodynamics. Based on similar thermodynamic principles, Jirasek and Zimmermann [12,30] used an integral type nonlocal damage model to predict micro-crack propagation and the transition to cohesive fracture debonding, in which the fracture was modeled by the embedded crack method. The energy equivalence is enforced at the local element, and the transition triggers when the local element strain across the embedded crack reaches a critical value. The same idea of energy equivalence at the tip element was adopted by Roth and collaborators [31], except that the transition could occur at any level of damage, and the integration-based nonlocal regularization was performed on stress instead of strain. In [13], macro fracture is modeled with traction free surfaces (no cohesive model) using the XFEM, and the transition happens when the gradient enhanced damage variable reaches unity. Comi and collaborators [14,32] coupled an integral type nonlocal damage model with a mode I cohesive zone model using the XFEM. The transition triggers at a certain damage threshold, which is not a constant: it is related to the size of the element at the fracture tip, and the energy equivalence is established by assigning to the cohesive zone model the same amount of energy as the energy not yet dissipated by the nonlocal model within the process zone. Wang and Waisman [16,33] extended this idea to mixed mode fracture propagation with damage–fracture transition. Recently, Cuvilliez and collaborators [15] designed a flexible modeling framework, in which the cohesive law is derived from the gradient damage model, and the transition from continuum damage to discrete cohesive fracture can happen at any level of damage. Leclerc and collaborators [34] further incorporated the effect of stress triaxiality into the macro cohesive zone model during the transition.

The numerical methods of transition from continuum damage to discrete fracture reviewed above have significant value; however, a few shortcomings still need to be addressed. First, in the diffused damage development phase, isotropic damage constitutive laws cannot account for anisotropic stiffness degradation due to the initiation of micro cracks in multiple directions. Anisotropic CDM models are necessary. Second, phenomenological damage cannot explicitly represent crack density evolution. Micromechanical damage models should be used for modeling multiscale fracture propagation. Third, the transition is the result of micro crack interaction and coalescence, hence the threshold value should be rigorously defined and calibrated.

In this paper, we couple a nonlocal micromechanics based damage model with a CZM by using the XFEM. In Section 2, we present an anisotropic CDM model in which the free enthalpy is obtained by integrating open and closed crack surface displacement jumps for a discrete set of crack orientations uniformly distributed on a unit sphere. We construct an equivalent strain variable to account for deformation induced by open cracks. We formulate a criterion to predict the evolution of the damage tensor in terms of equivalent strain. An integration based nonlocal regularization is employed to alleviate mesh dependence when cracks are open. In Section 3, we briefly introduce the Park–Paulino–Roesler (PPR) CZM [35], employed in this paper to characterize the macro cohesive fracture behavior. We rigorously calibrate the critical damage value that marks the transition from diffused micro-cracks to macro-fracture, as well as the strength and energy release rate of the PPR cohesive law. Constitutive laws at both micro- and macro-scales are coupled by employing the XFEM. In Section 4, we derive the strong and weak forms of the governing equations, we describe the algorithm used for computing the Jacobian and the macro-fracture tip advancement and we explain the state variables mapping technique. Wedge splitting and three-point bending tests are simulated to assess the performance of the proposed framework; results are presented in Section 5.

2. Micro-scale damage model

2.1. Derivation of the expression of the free energy

We adopt the expression of the free enthalpy established in [36–38] for a REV of volume Ω_r and external boundary $\partial \Omega_r$ subjected to a uniform stress $\boldsymbol{\sigma}$. It is assumed that penny shaped microscopic cracks of various
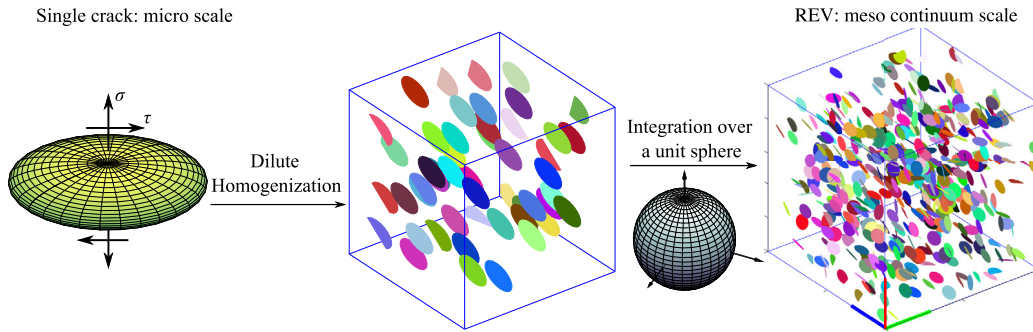
Fig. 1. Procedure to obtain the expression of the REV Gibbs free energy: (1) sum the elastic deformation energy stored in N cracks of same orientation; (2) integrate the result over the unit sphere to account for all possible crack orientations.

orientations are embedded in an isotropic linear elastic matrix of compliance tensor $\mathbb{S}_0$. Each microscopic crack is characterized by its normal direction $\overrightarrow{n}$ and its radius a. The macro strain of a REV that contains a single set of N microcracks oriented in planes normal to $\overrightarrow{n}$ is the sum of the elastic strain of the matrix and of the strains due to the normal and shear crack displacement jumps, as sketched in Fig. 1. We adopt a dilute homogenization scheme, in which it is assumed that microcracks do not interact. As explained in [39,40], the expression of the free enthalpy for a REV with a single set of N cracks is obtained as:

$$G^* = \frac{1}{2}\boldsymbol{\sigma} : \mathbb{S}_0 : \boldsymbol{\sigma} + \frac{1}{2}c_0\rho(\overrightarrow{n} \cdot \boldsymbol{\sigma} \cdot \overrightarrow{n})\langle \overrightarrow{n} \cdot \boldsymbol{\sigma} \cdot \overrightarrow{n}\rangle^+$$
$$+ \frac{1}{2}c_1\rho[(\boldsymbol{\sigma} \cdot \boldsymbol{\sigma}) : (\overrightarrow{n} \otimes \overrightarrow{n}) - \boldsymbol{\sigma} : (\overrightarrow{n} \otimes \overrightarrow{n} \otimes \overrightarrow{n} \otimes \overrightarrow{n}) : \boldsymbol{\sigma}] \tag{1}$$

in which we note $\langle x \rangle^+ = x, x \geq 0$, and $\langle x \rangle^+ = 0, x < 0$. The coefficient c_0 (respectively c_1) is defined as the normal (respectively shear) elastic compliance of the crack. $\rho(\overrightarrow{n})$ is the crack density, for the set of N cracks oriented in planes perpendicular to $\overrightarrow{n}$. We define:

$$c_0 = \frac{16}{3}\frac{1 - \nu_0^2}{E_0}, \quad c_1 = \frac{32}{3}\frac{1 - \nu_0^2}{(2 - \nu_0)E_0}, \quad \rho = \frac{Na^3}{|\Omega_r|} \tag{2}$$

where E_0 and ν_0 are the Young's modulus and Poisson's ratio of the matrix.

For several crack sets of different orientations, the Gibbs free energy of the REV is obtained by integrating G^* for a distribution of crack densities $\rho(\overrightarrow{n})$, over the unit sphere $S^2 = \{\overrightarrow{n}, |\overrightarrow{n}| = 1\}$ shown in Fig. 1, as follows:

$$G = \frac{1}{2}\boldsymbol{\sigma} : \mathbb{S}_0 : \boldsymbol{\sigma} + \frac{1}{8\pi}\int_{S^2}\{c_0\,\rho(\overrightarrow{n})(\overrightarrow{n} \cdot \boldsymbol{\sigma} \cdot \overrightarrow{n})\langle \overrightarrow{n} \cdot \boldsymbol{\sigma} \cdot \overrightarrow{n}\rangle^+$$
$$+ c_1\,\rho(\overrightarrow{n})[(\boldsymbol{\sigma} \cdot \boldsymbol{\sigma}) : (\overrightarrow{n} \otimes \overrightarrow{n}) - \boldsymbol{\sigma} : (\overrightarrow{n} \otimes \overrightarrow{n} \otimes \overrightarrow{n} \otimes \overrightarrow{n}) : \boldsymbol{\sigma}]\}dS \tag{3}$$

At the scale of the REV, the second order crack density tensor $\boldsymbol{\rho}$ is defined in such a way that: $\rho(\overrightarrow{n}) = \overrightarrow{n} \cdot \boldsymbol{\rho} \cdot \overrightarrow{n}$. The second order damage tensor is defined as follows:

$$\boldsymbol{\Omega} = \frac{1}{4\pi}\int_{S^2}\rho(\overrightarrow{n})(\overrightarrow{n} \otimes \overrightarrow{n})dS = \frac{1}{4\pi}\int_0^{2\pi}\int_0^{\pi}\rho(\overrightarrow{n})(\overrightarrow{n} \otimes \overrightarrow{n})sin\theta d\phi d\theta \tag{4}$$

It can be shown mathematically (see [37,41] for details) that the crack density function $\rho(\overrightarrow{n})$ is related to the damage tensor as follows:

$$\rho(\overrightarrow{n}) = \frac{3}{2}(5\overrightarrow{n} \cdot \boldsymbol{\Omega} \cdot \overrightarrow{n} - \text{Tr}\boldsymbol{\Omega}) \tag{5}$$

The free energy is the sum of the elastic deformation energy stored in the matrix and of the elastic energy stored in the displacement jumps across crack surfaces. Let us consider two particular cases: either all cracks are open ($\overrightarrow{n} \cdot \boldsymbol{\sigma} \cdot \overrightarrow{n} > 0$), or all cracks are closed ($\overrightarrow{n} \cdot \boldsymbol{\sigma} \cdot \overrightarrow{n} < 0$). After introducing the relation (5) in the expression of Gibbs energy and integrating over the unit sphere (Eq. (3)), we obtain the macroscopic free enthalpy as a function

of the second order damage tensor $\mathbf{\Omega}$, as follows:

$$
\begin{aligned}
G(\boldsymbol{\sigma}, \mathbf{\Omega}) = & \frac{1}{2} \boldsymbol{\sigma} : \mathbb{S}_0 : \boldsymbol{\sigma} + a_1 \operatorname{Tr}\mathbf{\Omega}(\operatorname{Tr}\boldsymbol{\sigma})^2 + a_2 \operatorname{Tr}(\boldsymbol{\sigma} \cdot \boldsymbol{\sigma} \cdot \mathbf{\Omega}) \\
& + a_3 \operatorname{Tr}\boldsymbol{\sigma} \operatorname{Tr}(\mathbf{\Omega} \cdot \boldsymbol{\sigma}) + a_4 \operatorname{Tr}\mathbf{\Omega} \operatorname{Tr}(\boldsymbol{\sigma} \cdot \boldsymbol{\sigma})
\end{aligned}
\tag{6}
$$

Please refer to Appendix for the details of the mathematical derivations. The four coefficients a_1, a_2, a_3 and a_4 are given as

$$
a_1 = \frac{-\mu}{140} c_1, \quad a_2 = \frac{7 + 2\mu}{14} c_1, \quad a_3 = \frac{\mu}{14} c_1, \quad a_4 = \frac{-\mu}{70} c_1
\tag{7}
$$

with $\mu = -\nu_0$ for open cracks and $\mu = -2$ for closed cracks. Note that the expression of the free enthalpy obtained from micro-mechanical principles in Eq. (6) is similar to that assumed in a number of purely phenomenological models, e.g. [42,43]. In the following, $\mu = -\nu_0$ for open cracks is used as we focus on modeling the propagation of a macro-fracture as a result from micro crack inception and growth.

The damage driving force (energy release rate), conjugated to the damage tensor, is defined as:

$$
\mathbf{Y} = \frac{\partial G(\boldsymbol{\sigma}, \mathbf{\Omega})}{\partial \mathbf{\Omega}} = a_1 (\operatorname{Tr}\boldsymbol{\sigma})^2 \boldsymbol{\delta} + a_2 \boldsymbol{\sigma} \cdot \boldsymbol{\sigma} + a_3 \operatorname{Tr}(\boldsymbol{\sigma})\boldsymbol{\sigma} + a_4 \operatorname{Tr}(\boldsymbol{\sigma} \cdot \boldsymbol{\sigma})\boldsymbol{\delta}
\tag{8}
$$

where the Kronecker symbol $\boldsymbol{\delta}$ stands for second order identity tensor. The stress/strain relation is obtained by thermodynamic conjugation:

$$
\begin{aligned}
\boldsymbol{\epsilon} = \frac{\partial G(\boldsymbol{\sigma}, \mathbf{\Omega})}{\partial \boldsymbol{\sigma}} = & \frac{1 + \nu_0}{E_0} \boldsymbol{\sigma} - \frac{\nu_0}{E_0}(\operatorname{Tr}\boldsymbol{\sigma})\boldsymbol{\delta} + 2a_1(\operatorname{Tr}\mathbf{\Omega} \operatorname{Tr}\boldsymbol{\sigma})\boldsymbol{\delta} + a_2(\boldsymbol{\sigma} \cdot \mathbf{\Omega} + \mathbf{\Omega} \cdot \boldsymbol{\sigma}) \\
& + a_3[\operatorname{Tr}(\boldsymbol{\sigma} \cdot \mathbf{\Omega})\boldsymbol{\delta} + (\operatorname{Tr}\boldsymbol{\sigma})\mathbf{\Omega}] + 2a_4(\operatorname{Tr}\mathbf{\Omega})\boldsymbol{\sigma}
\end{aligned}
\tag{9}
$$

2.2. Damage evolution and nonlocal regularization

Following Mazars and Pijaudier–Cabot [44], we define the local equivalent strain in terms of the positive principal strain components (noted $\langle \epsilon_I \rangle$), as:

$$
\hat{\epsilon} = \sqrt{\sum_{I=1}^{3} \langle \epsilon_I \rangle^2}
\tag{10}
$$

We consider linear hardening/softening in the damage criterion:

$$
f(\boldsymbol{\epsilon}, \mathbf{\Omega}) = \hat{\epsilon} - (\kappa + \eta \operatorname{Tr}\mathbf{\Omega})
\tag{11}
$$

where κ and η are material parameters. The damage evolution law is postulated so as to obtain damage patterns that conform to the observations as

$$
\dot{\mathbf{\Omega}} = \dot{\lambda} \mathbf{D} = \dot{\lambda}
\begin{bmatrix}
\langle \epsilon_1 \rangle^2 / \hat{\epsilon}^2 & 0 & 0 \\
0 & \langle \epsilon_2 \rangle^2 / \hat{\epsilon}^2 & 0 \\
0 & 0 & \langle \epsilon_3 \rangle^2 / \hat{\epsilon}^2
\end{bmatrix}.
\tag{12}
$$

We can easily verify that a uniaxial tensile loading in direction 1 can only result in cracks perpendicular to direction 1 because $\hat{\epsilon} = \epsilon_1 > 0$. The value of the Lagrangian multipliers $\dot{\lambda}$ is determined from consistency condition applied to the damage criterion (Eq. (11)):

$$
0 = \frac{\partial f}{\partial \hat{\epsilon}} \mathrm{d}\hat{\epsilon} + \frac{\partial f}{\partial \mathbf{\Omega}} : \mathrm{d}\mathbf{\Omega} = \dot{\hat{\epsilon}} - \eta \boldsymbol{\delta} : \dot{\mathbf{\Omega}}, \quad \rightarrow \dot{\lambda} = \dot{\hat{\epsilon}}/\eta \geq 0
\tag{13}
$$

According to the consistency equation, the damage rate $\dot{\Omega}$ is always non-negative. Since the damage driving force $\mathbf{Y}$ is positive definite (Eq. (8)), the positivity of energy dissipation is ensured, i.e., the second law of thermodynamics is satisfied:

$$
\mathbf{Y} : \dot{\mathbf{\Omega}} \geq 0
\tag{14}
$$

The formulated constitutive model yields strain softening behavior due to open micro crack evolution, which leads to the well known spurious localization and mesh dependency issues. A well-posed boundary value problem can be

recovered by utilizing localization limiters, formulated by integration or gradient based nonlocal regularization [45], micro-structure enrichment [46], or local adjustment of material properties based on element size and direction (crack band theory) [47]. In this paper, we use an integration-based nonlocal technique [48]: the evolution of the internal variables at a material point does not only depend on the stress and strain at that point, but also on the field variables within an influence domain surrounding that point. The size of the nonlocal influence domain is controlled by a characteristic internal length l_c, which is a material parameter usually equal to 2 to 3 times the maximum size of grains encountered in a polycrystal [49]. Mathematically, we replaced the equivalent strains that control damage evolution (Eq. (10)) by their weighted average defined on an influence domain V, as follows:

$$\hat{\epsilon}^{nl}(\boldsymbol{x}) = \int_V \omega(\boldsymbol{x}, \boldsymbol{\xi}) \hat{\epsilon}(\boldsymbol{\xi}) \mathbf{d} V(\boldsymbol{\xi}) \tag{15}$$

where $\boldsymbol{x}$ is the position vector of the material point considered, and $\boldsymbol{\xi}$ is the position vector of points in the influence domain of $\boldsymbol{x}$. $\omega(\boldsymbol{x}, \boldsymbol{\xi})$ is the nonlocal weight function, which decreases monotonically as the distance $r = \|\boldsymbol{x} - \boldsymbol{\xi}\|$ increases. Note that if field variables are uniform, the value of damage should be uniform. Hence the nonlocal value of the equivalent strains should be equal to the local value of equivalent strains in the uniform strain field. This implies that weight functions should satisfy the partition of unity: $\int_V \omega(\boldsymbol{x}, \boldsymbol{\xi}) \mathbf{d} V(\boldsymbol{\xi}) = 1$. Accordingly, weight functions usually take the following general form:

$$\omega(\boldsymbol{x}, \boldsymbol{\xi}) = \frac{\omega_0(\boldsymbol{x}, \boldsymbol{\xi})}{\int_V \omega_0(\boldsymbol{x}, \boldsymbol{\xi}) \mathbf{d} V(\boldsymbol{\xi})} = \frac{\omega_0(\boldsymbol{x}, \boldsymbol{\xi})}{V_r(\boldsymbol{x})} \tag{16}$$

where $V_r(\boldsymbol{x})$ is the so-called characteristic volume. The exact form of the weight function $\omega_0(\boldsymbol{x}, \boldsymbol{\xi})$ depends on the material considered. The Gauss function (normal distribution) and the bell-shaped function are the most widely used weight functions for isotropic media. Here, we adopt the bell-shaped function, expressed as:

$$\omega_0(r) = \left\langle 1 - \frac{r^2}{l_c^2} \right\rangle^2. \tag{17}$$

The advantage of the bell-shaped function is that the nonlocal influence zone only depends on l_c: no cut-off is needed to ensure that the weight function is zero outside of the influence zone. In the FEM, nonlocal variables are calculated as the weighted average of local variables obtained iteratively at the Gauss points located in the influence zone [18,38]. For instance, the nonlocal equivalent strain is expressed as:

$$\hat{\epsilon}^{nl}(\boldsymbol{x}) = \frac{\sum_{j=1}^{N_{GP}} \omega_0(\|\boldsymbol{x} - \boldsymbol{\xi}_j\|) \hat{\epsilon}(\boldsymbol{\xi}_j) \Delta V_j}{\sum_{j=1}^{N_{GP}} \omega_0(\|\boldsymbol{x} - \boldsymbol{\xi}_j\|) \Delta V_j} \tag{18}$$

where N_{GP} the total number of Gauss points inside the influence zone of material point $\boldsymbol{x}$. ΔV_j is the integration volume associated with the jth Gauss point.

Note that the proposed model does not consider inelastic/plastic deformation. The monotonic increase in damage (micro-crack density) only contributes to the degradation of material stiffness. When the material is unloaded, the opened micro-cracks close. The unloading path is a straight line to the point of zero stress and zero strain. The slope of that line corresponds to the damaged stiffness of the REV. Additionally, the tangent stiffness, defined as the derivative of stress by strain, has additional terms that stem from the non-local regularization. When these second-order terms are dropped, the expression of stiffness boils down to that of the secant stiffness, which means that the quadratic convergence rate of the global iteration scheme is lost.

3. Coupling cohesive fracture propagation with continuum damage zone evolution

3.1. Critical damage threshold calibration

The constitutive model proposed in Section 2, based on a dilute homogenization scheme, relates macro-scale stress–strain behavior with micro-scale crack density, as long as crack interactions can be neglected. Crack interaction is followed by crack coalescence and macro-fracture formation. Macro-scale fracture propagation cannot be predicted by CDM and requires a fracture mechanics approach based on the concept of stress-intensity factor, energy release rate, Crack Tip Opening Displacement (CTOD) or Crack Mouth Opening Displacement (CMOD). In this paper, a CZM is adopted to capture the softening induced by the separation of macro-fracture surfaces. We
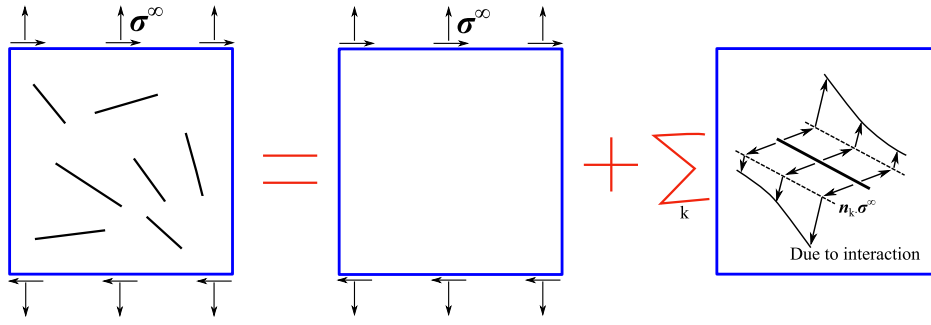
Fig. 2. Crack interaction model in Kachanov's theory.

start by calibrating the critical damage (i.e., crack density) which marks the transition between continuum damage propagation and macro-fracture formation. To this aim, we calculate the damaged Young's modulus of a 2D REV that contains one set of parallel equally sized cracks, by using two methods: first, the proposed continuum damage model, which does not account for micro-crack interaction; second, Kachanov's micro-mechanical model [50], which accounts for micro-crack interaction. The critical damage value is defined as the level of damage above which the predictions of damaged elastic stiffness differ in the two models. Details are provided below.

In the 2D micro-mechanical damage model proposed by Kachanov, the stress and strain fields in a linear elastic plate containing N cracks, subjected to the stress σ^∞ at infinity, are calculated as those in a plate subjected to zero far field stress and containing N loaded micro-cracks. The faces of each micro-crack ($i = 1, \ldots, N$) are subjected to the traction $t_i^0 = n_i \cdot \sigma^\infty$, in which n_i is the unit vector normal to the faces of the ith crack. According to the superposition theory for elastic media, this problem can be solved by considering N plates containing only one crack subjected to the traction t_i ($i = 1, \ldots, N$), defined as the sum of t_i^0 and the additional tractions due to stress interactions with the other micro-cracks. The superposition method is illustrated in Fig. 2. The tractions can be determined by solving a system of integral equations, as follows [50]:

$$t_i(\zeta_i) = t_i^0 + n_i \cdot \sum_{j \neq i} \int_{-l_j}^{l_j} \sigma_j^n(\zeta_i, \zeta_j)[n_j \cdot t_j(\zeta_j)] + \sigma_j^\tau(\zeta_i, \zeta_j)[\tau_j \cdot t_j(\zeta_j)]d\zeta_j \tag{19}$$

in which l_j is the half length of the jth crack and τ_j is the unit vector that is tangential to the faces of the jth crack. $\sigma_j^n(\zeta_i, \zeta_j)$ (respectively $\sigma_j^\tau(\zeta_i, \zeta_j)$) is the stress tensor at the current point ζ_i on the ith crack, generated by a pair of equal and opposite unit forces located at point ζ_j along the normal (respectively tangential) direction of the jth crack. Following the approximation proposed and validated by Kachanov [50], we can obtain the tractions $t_i(\zeta_i)$ by solving the system of Eqs. (19). The detailed procedure is provided in [51].

The average relative displacement vector $\langle b_i \rangle$ across the faces of the ith crack is found by superposing the displacements due to punctual tractions at each point of the ith crack faces [50]:

$$\langle b_i \rangle = \frac{4l_i}{E_0} \int_{-l_i}^{l_i} t_i(\zeta_i)[1 - (\zeta_i/l_i)^2]^{1/2}d\zeta_i \tag{20}$$

in which E_0 is the Young's modulus of the matrix (bounding material) between the cracks. The fourth order effective compliance tensor $\mathbb{S}^{eff}$ is used to relate the average strain $\langle \epsilon \rangle$ to the applied far field stress σ^∞ over a representative area A:

$$\langle \epsilon \rangle = \mathbb{S}^{eff} : \sigma^\infty = \mathbb{S}_0 : \sigma^\infty + \frac{1}{2A} \sum_{i=1}^{N} \int_{-l_i}^{l_i} [n_i(\zeta_i)b_i(\zeta_i) + b_i(\zeta_i)n_i(\zeta_i)]d\zeta_i \tag{21}$$

where $\mathbb{S}^0$ is elastic compliance tensor without cracks, and $n_i(\zeta_i)$ is the unit vector normal to the ith crack face at point ζ_i. We consider flat cracks, for which $n_i(\zeta_i)$ is a constant. Eq. (21) thus becomes:

$$\langle \epsilon \rangle = \mathbb{S}_0 : \sigma^\infty + \frac{l_i}{A} \sum_{i=1}^{N} [n_i \langle b_i \rangle + \langle b_i \rangle n_i] \tag{22}$$
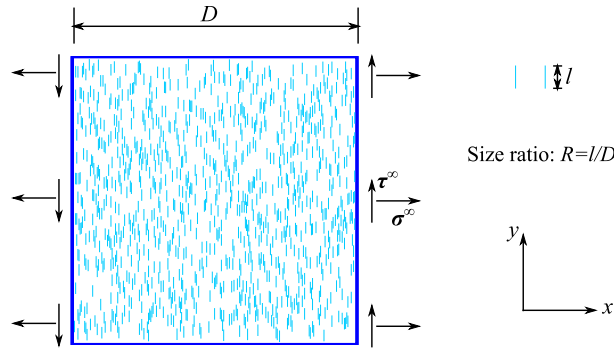
Fig. 3. Random crack pattern adopted to calculate the reduction of stiffness due to damage in the proposed CDM model and in Kachanov's theory.

The expressions of the stress distributions that are involved in the integral terms of Eqs. (19) and (20) are very complex, which makes it challenging to obtain the exact solution of the traction and displacement distributions along each crack face. To overcome this problem, several approximation methods were proposed [50,52–54]. In the following, we adopt Kachanov's approximation method [50], in which Eq. (20) is written as follows:

$$\langle \boldsymbol{b}_i \rangle = \frac{\pi \, l_i}{E_0} \langle \boldsymbol{t}_i \rangle \tag{23}$$

where $\langle \boldsymbol{t}_i \rangle$ is the mean traction field that applies to the ith crack.

In the following, we consider a 2D REV that contains cracks perpendicular to the x-axis, and we calculate the Young's modulus in the x-direction. We randomly populate the crack centers inside the REV as shown Fig. 3. The crack density in Kachanov's model (ρ) is defined in the same way as in the proposed CDM model (Eq. (2)). But since the problem solved here is in 2D, the crack surface area and the REV volume are replaced by the crack length and the REV area, respectively. As a result:

$$\Omega_{xx} = \rho_x = \frac{1}{A} \sum_{i=1}^{N} l_i^2 \tag{24}$$

In the present case, because all the cracks are perpendicular to the x-axis, the elastic moduli are affected by the crack density (ρ_x) in Kachanov's model, and by the $xx-$ component of the damage tensor (Ω_{xx}) in the continuum damage model. We simulated a simple tensile test at the material point with the continuum model. The effective Young's modulus along the x-direction (solid black line in Fig. 4) was obtained from the compliance tensor, as follows:

$$\mathbb{S} = \frac{\partial^2 G(\boldsymbol{\sigma}, \boldsymbol{\Omega})}{\partial \boldsymbol{\sigma}^2} \tag{25}$$

where G is Gibbs free energy expressed in Eq. (6). We calculated the damaged elastic tensor with Kachanov's model for several values of crack density, by either increasing the number of cracks in the REV with a fixed crack length (crack initiation), or by increasing the length of a fixed number of cracks in the REV (crack propagation). Note that in all simulations, the centers of the cracks were randomly distributed inside the REV, with non-overlap and non-intersection constraints. To ensure that the domain of size D remained a REV, we used a ratio $R = l/D$ of 1/25.

Fig. 4 shows the evolution of effective modulus E_{xx}^{eff} as the crack density (damage) in the x-axis increases, for two different initial moduli. It is worth noting that the value of the damaged Young's modulus only depends on crack density — and not on the type of damage growth (crack initiation vs. crack propagation). Since the free energy expression (Eq. (6)) is calculated from a dilute homogenization scheme, the effective modulus predicted by the continuum model (solid black line) coincides with that predicted by Kachanov's model (markers & red dashed line) until crack density exceeds $\Omega_{xx}^{eff} = \rho_x = 0.2$. When crack density exceeds 0.2, the modulus degradation rate predicted by Kachanov's theory is lower than in the CDM model, because of stress shadowing effects (due to crack interactions). Moreover, the point that marks the divergence between the two models does not depend on the initial modulus used for calculation (case 1 vs. case 2). In summary, $\Omega_{crit} = 0.2$ is the limit value above which
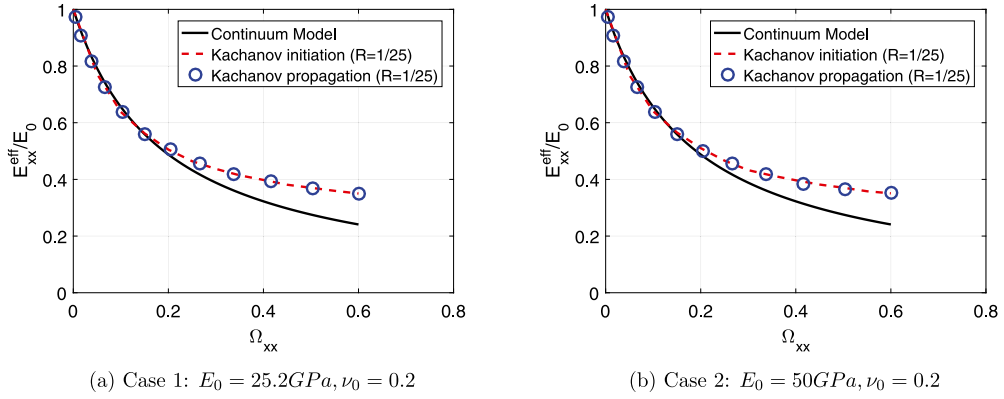
(a) Case 1: $E_0 = 25.2 GPa, \nu_0 = 0.2$ (b) Case 2: $E_0 = 50 GPa, \nu_0 = 0.2$

Fig. 4. Damaged Youngs' modulus calculated with the continuum model and with Kachanov's micro-mechanical model for a set of cracks perpendicular to the x-axis.
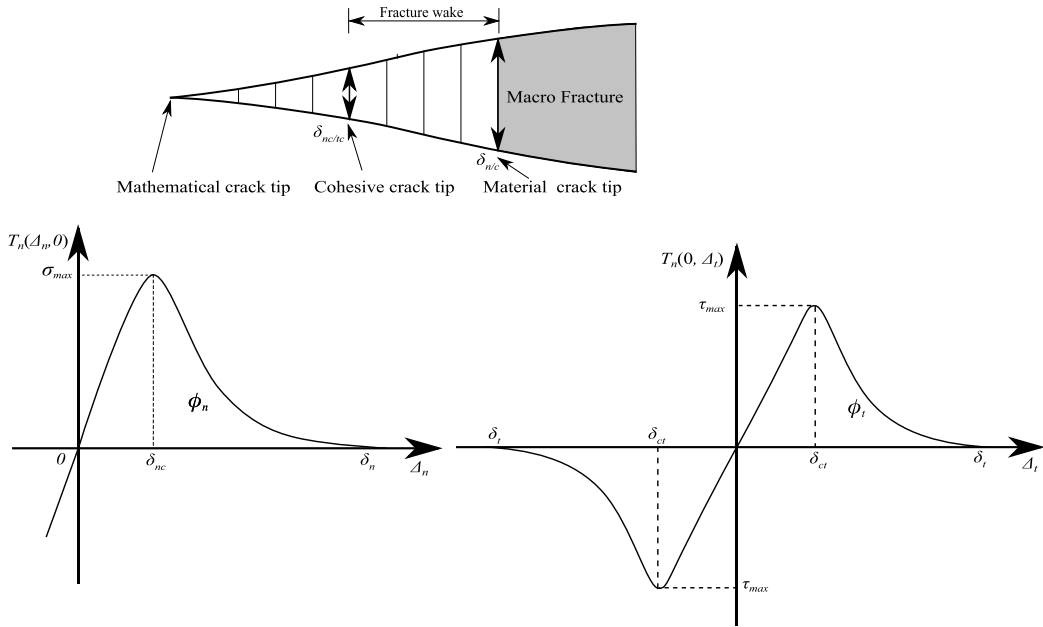

Fig. 5. PPR cohesive model of macro-fracture propagation.

the interaction between micro cracks cannot be ignored: it marks the transition from diffused micro-scale cracks to concentrated macro-fracture.

3.2. Macro-scale cohesive zone model: PPR

Above the critical damage threshold $\Omega_{crit} = 0.2$, the continuum assumption is not valid any longer, and damage needs to be replaced by a macro-fracture segment in the FEM model. We use a CZM governed by a traction–separation law to represent the macro fracture. In this paper, we list the main equations of the potential based Park–Paulino–Roesler (PPR) [35] cohesive model, adopted here. The PPR model is different from non-potential based cohesive zone models, in which *ad hoc* traction–separation laws are defined in terms of effective displacement. As a result, the PPR model guarantees that the tangent stiffness within the softening region is negative, and does not exhibit any non-physical interface behavior under complex loading conditions [55].

In the PPR cohesive zone model [35], a unified potential is constructed so as to meet the following requirements: (i) Complete normal and shear failure are reached when either the normal or the tangential separation reaches a maximum value; (ii) The traction rate is equal to zero when the traction is equal to the cohesive strength; (iii) The energy release rate is equal to the area enclosed by the traction–separation curve.

The expression of the potential is

$$
\Psi(\Delta_n, \Delta_t) = \min(\phi_n, \phi_t) + \left[\Gamma_n \left(1 - \frac{\Delta_n}{\delta_n} \right)^{\alpha} \left(\frac{m}{\alpha} + \frac{\Delta_n}{\delta_n} \right)^{m} + \langle \phi_n - \phi_t \rangle \right]
$$
$$
\times \left[\Gamma_t \left(1 - \frac{|\Delta_t|}{\delta_t} \right)^{\beta} \left(\frac{n}{\beta} + \frac{|\Delta_t|}{\delta_t} \right)^{n} + \langle \phi_t - \phi_n \rangle \right].
$$

(26)

where Δ_n and Δ_t (respectively δ_n and δ_t) stand for the separations in the normal and shear directions at the current time (respectively, at failure) as shown in Fig. 5. ϕ_n (respectively ϕ_t) is the mode I (respectively, mode II) cohesive energy release rate. α and β are the shape factors that control the concave or convex nature of the softening curve. The mechanical response of brittle materials is best represented by power law softening equations or bilinear softening laws [56]. Accordingly, we use $\alpha = \beta = 4$, which allows representing concave shaped softening curves with a power law. The traction vector (T_n, T_t) is obtained directly from the derivative of the potential in Eq. (26):

$$
T_n(\Delta_n, \Delta_t) = \frac{\Gamma_n}{\delta_n} \left[m \left(1 - \frac{\Delta_n}{\delta_n} \right)^{\alpha} \left(\frac{m}{\alpha} + \frac{\Delta_n}{\delta_n} \right)^{m-1} - \alpha \left(1 - \frac{\Delta_n}{\delta_n} \right)^{\alpha-1} \left(\frac{m}{\alpha} + \frac{\Delta_n}{\delta_n} \right)^{m} \right]
$$
$$
\times \left[\Gamma_t \left(1 - \frac{|\Delta_t|}{\delta_t} \right)^{\beta} \left(\frac{n}{\beta} + \frac{|\Delta_t|}{\delta_t} \right)^{n} + \langle \phi_t - \phi_n \rangle \right]
$$
$$
T_t(\Delta_n, \Delta_t) = \frac{\Gamma_t}{\delta_t} \left[n \left(1 - \frac{|\Delta_t|}{\delta_t} \right)^{\beta} \left(\frac{n}{\beta} + \frac{|\Delta_t|}{\delta_t} \right)^{n-1} - \beta \left(1 - \frac{|\Delta_t|}{\delta_t} \right)^{\beta-1} \left(\frac{n}{\beta} + \frac{|\Delta_t|}{\delta_t} \right)^{n} \right]
$$
$$
\times \left[\Gamma_n \left(1 - \frac{\Delta_n}{\delta_n} \right)^{\alpha} \left(\frac{m}{\alpha} + \frac{\Delta_n}{\delta_n} \right)^{m} + \langle \phi_n - \phi_t \rangle \right] \frac{\Delta_t}{|\Delta_t|}
$$

(27)

where Γ_n and Γ_t are energy constants, related to ϕ_n and ϕ_t as follows:

$$
\Gamma_n = (-\phi_n)^{\langle \phi_n - \phi_t \rangle / (\phi_n - \phi_t)} \left(\frac{\alpha}{m} \right)^{m}, \quad \Gamma_t = (-\phi_t)^{\langle \phi_t - \phi_n \rangle / (\phi_t - \phi_n)} \left(\frac{\beta}{n} \right)^{n}.
$$

(28)

where m, n, called the non-dimensional exponents, are expressed in terms of the constant shape factors α, β and of the initial slope indicators (λ_n, λ_t), as follows:

$$
m = \frac{\alpha(\alpha - 1)\lambda_n^2}{(1 - \alpha\lambda_n^2)}, \quad n = \frac{\beta(\beta - 1)\lambda_t^2}{(1 - \beta\lambda_t^2)}
$$

(29)

The initial slope indicators are defined as the ratios of critical crack opening width to the final crack opening width (Fig. 5), i.e. $\lambda_n = \delta_{nc}/\delta_n$, $\lambda_t = \delta_{tc}/\delta_t$. Usually, the extrinsic CZM, in which the elastic behavior (or initial ascending slope) is excluded, is used to model fracture propagation when a cohesive segment or a cohesive interface element is adaptively inserted. Only the softening branch is used, because the elastic deformation of the material is already accounted for by the continuum model. However, numerical simulations indicate that the absence of one-to-one relationship at the point $\Delta_n = \Delta_t = 0$ causes stability issues. In the following, we use the intrinsic cohesive zone model with $\lambda_n = \lambda_t = 0.001$ to improve the convergence rate, and to avoid unwanted elastic separation.

To close the formulation of the PPR cohesive model, relationships between the cohesive strengths $(\sigma_{\max}, \tau_{\max})$ and the final normal and shear crack opening widths (δ_n, δ_t) are needed. The traction rate is equal to zero when traction is equal to the cohesive strength, so we have:

$$
\delta_n = \frac{\phi_n}{\sigma_{\max}} \alpha \lambda_n \left(1 - \lambda_n \right)^{\alpha-1} \left(\frac{\alpha}{m} + 1 \right) \left(\frac{\alpha}{m} \lambda_n + 1 \right)^{m-1}
$$
$$
\delta_t = \frac{\phi_t}{\tau_{\max}} \beta \lambda_t \left(1 - \lambda_t \right)^{\beta-1} \left(\frac{\beta}{n} + 1 \right) \left(\frac{\beta}{n} \lambda_t + 1 \right)^{n-1}
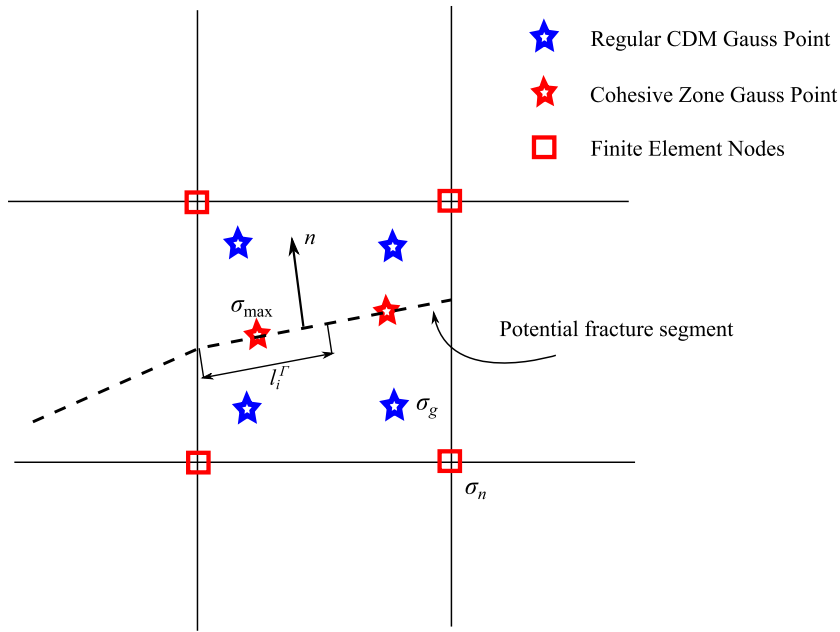$$

(30)

Fig. 6. Numerical method employed to determine the CZM PPR cohesive strength.

Different from monotonic loading, the potential is not directly used for unloading and reloading. Following the strategy presented in [35,57], a scaled linear relationship is adopted and implemented, as follows:

$$
\begin{aligned}
T_n^u(\Delta_n, \Delta_t) &= T_n(\Delta_{n_{\max}}, \Delta_t) \frac{\Delta_n}{\Delta_{n_{\max}}} \\
T_t^u(\Delta_n, \Delta_t) &= T_t(\Delta_n, \Delta_{t_{\max}}) \frac{\Delta_t}{\Delta_{t_{\max}}}
\end{aligned}
\tag{31}
$$

where $\Delta_{n_{\max}}$ (respectively, $\Delta_{t_{\max}}$) is the maximum normal (respectively, absolute tangential) separation ever reached in the loading history. Note that we adopted the penalty stiffness approach to model fracture surface contact behavior. As explained in [58], the tangent Jacobian matrix can be calculated analytically in the potential based CZM, which is critical to achieve quadratic convergence in FEM simulations. The reader is referred to [35,57] for the expression of the Jacobian matrix for loading, unloading, and reloading phases.

3.3. Cohesive strength and energy release rate of the PPR CZM

The cohesive zone model presented in Section 3.2 for pure mode I macro fracture propagation requires 4 material parameters. Here, we consider that the shape factors are $\alpha = \beta = 4$ and that the initial slope indicator are $\lambda_n = \lambda_t = 0.001$ - these values are typical for brittle materials. As a result, only the cohesive strength $\sigma_{\max}$ and the cohesive energy release rate ϕ_n need to be calibrated. The transition from an element with diffuse damage at $\Omega_{crit} = 0.2$ to an element with a cohesive fracture is handled by writing the equilibrium of forces before and after the separation of the damaged element. The cohesive strength at a Gauss Point along the cohesive segment should equal the projected stress interpolated from the stress state of the element, as shown in Fig. 6. Numerically, we first obtain the stress tensor σ_n at all the nodes of the element from the stress state σ_g of the Gauss Points, according to the procedure described in Section 4.4. Then, we use the shape functions to interpolate the stress state at the location of the Gauss points of the cohesive zone (see Section 4.3 for details on how to find the position of the newly created cohesive segment). Finally, we multiply the interpolated stress tensor by the normal unit vector orthogonal to the fracture segment $\overrightarrow{n}$ to obtain the cohesive strength $\sigma_{\max}$.

For the cohesive energy release rate, we adopt the method described in [16], which ensures that the energy dissipated for propagating a unit area of fracture is the same for the CZM alone and for the CZM coupled to the
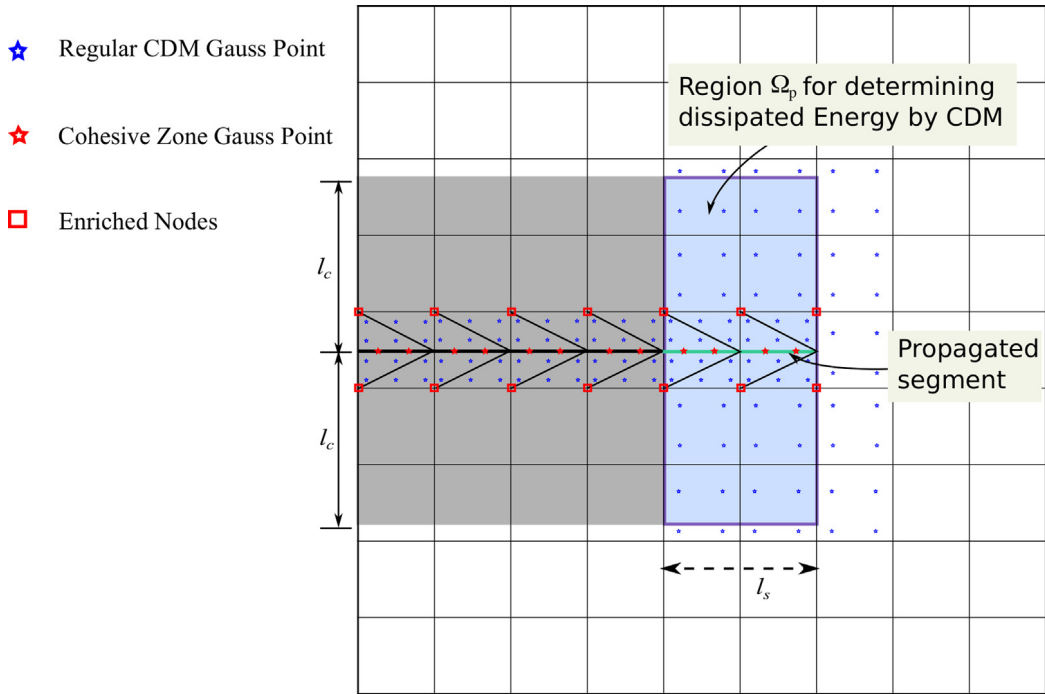
Fig. 7. Numerical method employed to determine cohesive energy release rate. (For interpretation of the references to color in this figure legend, the reader is referred to the web version of this article.)

nonlocal CDM model. Mathematically, this energy equivalence is expressed as

$$\int_0^t \sum_{i=1}^{N_{cz}} G_f l_i^\Gamma \mathrm{d}\tau = \int_0^t \sum_{i=1}^{N_{cz}} \phi_i l_i^\Gamma \mathrm{d}\tau + E_\Omega \tag{32}$$

where G_f is the fracture energy release rate measured from laboratory experiments, in which the creation of macro-scale fracture surfaces is assumed to be the only source of energy dissipation. l_i^Γ is the fracture length in 2D (or fracture surface area in 3D) associated with the Gauss Point i as shown in Fig. 6. N_{cz} is the total number of cohesive Gauss Points in the system. E_Ω represents the amount of energy dissipated by diffused damage development within the process zone, expressed as:

$$E_\Omega = \int_0^t \int_{\Omega_p} \boldsymbol{\sigma} : \dot{\boldsymbol{\epsilon}} d\Omega \mathrm{d}\tau - \frac{1}{2} \int_{\Omega_p} \boldsymbol{\sigma} : \boldsymbol{\epsilon} d\Omega. \tag{33}$$

Numerically, we first use Eq. (33) to calculate the total energy released by continuum damage development within the process zone Ω_p (shaded in blue in Fig. 7). The size of the process zone in the direction perpendicular to the macro fracture is related to the nonlocal internal length parameter l_c. Here, the width of the process zone size is equal to $2 \times l_c$ because the nonlocal weight function is bell-shaped (i.e., the weight function is zero beyond a distance l_c). Through Eq. (33), it is also assumed that the previously developed process zone (shaded in gray) is frozen after the transition from continuum damage to cohesive fracture. In other words, the elements in the shaded gray area are governed by a linear elastic constitutive function with reduced stiffness $\mathbb{C}(\Omega_{crit})$; no more energy dissipation comes from those bulk elements. Furthermore, we note that the length (area in 3D) of the newly formed cohesive segments is l_s, which indicates that the energy that should be dissipated to create the correct amount of fracture surfaces is $G_f l_s$. We use Eq. (32) to obtain the energy release rate for each cohesive Gauss point, as
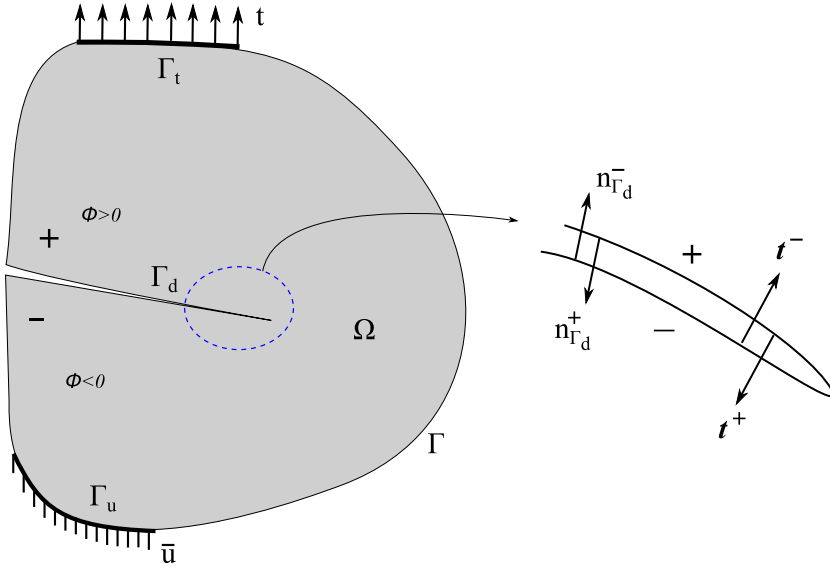
$$\phi_n = G_f - E_\Omega / l_s. \tag{34}$$

Fig. 8. Boundary conditions imposed on the domain of the bulk, Ω, and on the macro-fracture Γ_d. Note the level set function $\phi(\boldsymbol{x})$ is defined as the normal distance to the fracture surface/curve, using the same sign (positive/negative) as fracture surfaces (Γ_d^+, Γ_d^-). Accordingly, the location of the fracture is defined mathematically by $\phi(\boldsymbol{x}) = 0$.

4. Numerical implementation

4.1. Governing equation

Consider a domain Ω, as shown in Fig. 8, containing a fracture Γ_d. A prescribed traction $\bar{\boldsymbol{t}}$ is imposed on the boundary Γ_t and a prescribed displacement $\bar{\boldsymbol{u}}$ is imposed on the boundary Γ_u. Along the boundary of the macro-fracture, positive and negative cohesive tractions ($\boldsymbol{t}^+, \boldsymbol{t}^-$) are imposed on the positive and negative surfaces (Γ_d^+, Γ_d^-). The equilibrium governing equation and the associated natural boundary conditions are expressed as:

$$
\begin{aligned}
&\nabla \cdot \boldsymbol{\sigma} + \boldsymbol{b} = 0 \quad \text{in} \quad \Omega \\
&\boldsymbol{\sigma} \cdot \boldsymbol{n} = \bar{\boldsymbol{t}} \quad \text{on} \quad \Gamma_t \\
&\boldsymbol{\sigma} \cdot \boldsymbol{n}_{\Gamma_d}^+ = -\boldsymbol{\sigma} \cdot \boldsymbol{n}_{\Gamma_d}^- = \boldsymbol{t}^+ = -\boldsymbol{t}^- = \boldsymbol{t}(T_n, T_t) \quad \text{on} \quad \Gamma_d
\end{aligned}
\tag{35}
$$

where $\boldsymbol{\sigma}$ is the Cauchy stress tensor and $\boldsymbol{b}$ is the body force per unit volume. $\boldsymbol{n}$ is the outward normal unit vector on the outer boundary, $\boldsymbol{n}_{\Gamma_d}^+$ and $\boldsymbol{n}_{\Gamma_d}^-$ are the outward normal to the fracture boundary, from the positive and negative subdomains, respectively (see Fig. 8). The kinematic equations include the strain–displacement relationship, the definition of cohesive separation and the essential boundary conditions, as follows:

$$
\begin{aligned}
&\boldsymbol{\epsilon} = \nabla \boldsymbol{u} \quad \text{in} \quad \Omega \\
&[\![\boldsymbol{u}]\!](\Delta_n, \Delta_t) = \boldsymbol{u}^- - \boldsymbol{u}^+ \quad \text{on} \quad \Gamma_d \\
&\boldsymbol{u} = \bar{\boldsymbol{u}} \quad \text{on} \quad \Gamma_u
\end{aligned}
\tag{36}
$$

Finally, we relate the stress $\boldsymbol{\sigma}$ with the strain $\boldsymbol{\epsilon}$ and the cohesive traction $\boldsymbol{t}$ with the separation $[\![\boldsymbol{u}]\!]$ through the constitutive laws developed in Sections 2 and 3.2, and formally written as:

$$
\begin{aligned}
&\boldsymbol{\sigma} = \mathbb{C}(\boldsymbol{\Omega}) : \boldsymbol{\epsilon} = \mathbb{S}^{-1}(\boldsymbol{\Omega}) : \boldsymbol{\epsilon} \quad \text{in} \quad \Omega \\
&\boldsymbol{t}(T_n, T_t) = \boldsymbol{K}_{coh} [\![\boldsymbol{u}]\!](\Delta_n, \Delta_t) \quad \text{on} \quad \Gamma_d
\end{aligned}
\tag{37}
$$

where $\mathbb{C} = \mathbb{S}^{-1}$ is the fourth-order stiffness tensor. $\boldsymbol{K}_{coh}$ is the second-order stiffness tensor of the cohesive zone (i.e. the stiffness in the separation law).

In order to implement the governing equation into a finite element code, the strong form of the governing equations above needs to be transformed into a weak form. We multiply the equilibrium equations by a virtual

displacement function $\delta \boldsymbol{u}$ and integrate it over the whole domain Ω. After utilizing the divergence theorem and the boundary conditions, we have the weak form as:

$$\int_{\Omega} \nabla \delta \boldsymbol{u} : \boldsymbol{\sigma} \mathrm{d}\Omega + \int_{\Gamma_d} \delta [\![\boldsymbol{u}]\!] \cdot \boldsymbol{t} \mathrm{d}\Gamma = \int_{\Gamma_t} \delta \boldsymbol{u} \cdot \bar{\boldsymbol{t}} \mathrm{d}\Gamma + \int_{\Omega} \delta \boldsymbol{u} \cdot \boldsymbol{b} \mathrm{d}\Omega, \quad \forall \delta \boldsymbol{u} \in V \tag{38}$$

where V represents the space of all possible displacement fields that satisfy $\delta \boldsymbol{u} = 0$ on Γ_u.

4.2. XFEM discretization

Simulating fracture propagation without imposing a predefined fracture path is a long-standing issue. Techniques employed in engineering include: inserting interface elements to the boundaries of all regular finite elements prior to the loading simulation [59,60], dynamically inserting interface elements to the fracture path during the simulation [22,61], and using the eXtended Finite Element Method (XFEM) in which extra degrees of freedom are added to the nodes of the elements where the fracture passes through [62], based on the concept of partition of unity [63]. In this paper, we adopt the XFEM to discretize the primary variable, the displacement field. Note that the classical branch functions which are used to approximate the near tip stress singularity are not used here, because the stress singularity does not exist in the coupled CDM–CZM framework. Only the Heaviside jump function is used. Consequently, the approximation of the displacement field reads:

$$\boldsymbol{u}^h(\boldsymbol{x}) = \sum_{i \in S} N_i(\boldsymbol{x}) \boldsymbol{u}_i + \sum_{i \in S_H} N_i(\boldsymbol{x}) \frac{1}{2} [H(\boldsymbol{x}) - H(\boldsymbol{x}_i)] \boldsymbol{a}_i, \quad \forall \boldsymbol{x} \in \Omega$$
$$= \boldsymbol{N}_u(\boldsymbol{x}) \boldsymbol{U} + \boldsymbol{N}_a(\boldsymbol{x}) \boldsymbol{A} \tag{39}$$

in which S is the set of all nodal points and S_H is the set of enriched nodes that constitute elements bisected by the fracture. $\boldsymbol{u}_i$ and $\boldsymbol{a}_i$ denote the nodal values of the displacement field associated with the standard and enriched degrees of freedom (DOF), respectively. $N_i(\boldsymbol{x})$ is the standard shape function associated with node i, and the Heaviside jump function $H(\boldsymbol{x})$ is defined as

$$H_{\Gamma_d}(\boldsymbol{x}) = \begin{cases} +1, & \phi(\boldsymbol{x}) > 0 \\ -1, & \phi(\boldsymbol{x}) < 0 \end{cases} \tag{40}$$

where $\phi(\boldsymbol{x})$ is the level set function, the definition of which is illustrated in Fig. 8. It is worth noting that we shift the jump function in Eq. (39), to avoid the problem of post processing for blending elements [64]. By substituting the values of the Heaviside definition in Eq. (39), we obtain the following form of the displacement jump:

$$[\![\boldsymbol{u}(\boldsymbol{x}, t)]\!] = \sum_{i \in S_H} N_i(\boldsymbol{x}) \boldsymbol{a}_i = \boldsymbol{N}_u(\boldsymbol{x}) \boldsymbol{A} \tag{41}$$

By substituting the approximation functions (39)–(41) into the weak form of the governing equation (38), the following discretized residual equations can be obtained:

$$\boldsymbol{R}^u = \boldsymbol{F}_u^{\text{int}} - \boldsymbol{F}_u^{\text{ext}} = 0$$
$$\boldsymbol{R}^a = \boldsymbol{F}_a^{\text{int}} + \boldsymbol{F}^{\text{coh}} - \boldsymbol{F}_a^{\text{ext}} = 0 \tag{42}$$

in which we used Voigt notations. $\boldsymbol{F}_\alpha^{\text{int}}$, $\boldsymbol{F}_\alpha^{\text{ext}}$ and $\boldsymbol{F}^{\text{coh}}$ are the internal force vector, the external force vector and the cohesive force vector respectively, defined as:

$$\boldsymbol{F}_\alpha^{\text{int}} = \int_{\Omega} \boldsymbol{B}_\alpha^T \boldsymbol{\sigma} \mathrm{d}\Omega$$
$$\boldsymbol{F}_\alpha^{\text{ext}} = \int_{\Gamma_t} \boldsymbol{N}_\alpha \bar{\boldsymbol{t}} \mathrm{d}\Gamma + \int_{\Omega} \boldsymbol{N}_\alpha \boldsymbol{b} \mathrm{d}\Omega \tag{43}$$
$$\boldsymbol{F}^{\text{coh}} = \int_{\Gamma_d} \boldsymbol{N}_u \boldsymbol{\Lambda}^T \boldsymbol{t}(T_n, T_t) \mathrm{d}\Gamma$$

where $\boldsymbol{B}_\alpha$ represents the derivatives of the shape functions, as follows:

$$\boldsymbol{B}_\alpha = \begin{bmatrix} N_{\alpha,x} & 0 \\ 0 & N_{\alpha,y} \\ N_{\alpha,y} & N_{\alpha,x} \end{bmatrix}, \tag{44}$$

and $\mathbf{\Lambda}$ is the rotation matrix defined as

$$\mathbf{\Lambda} = \begin{bmatrix} \cos\theta & \sin\theta \\ -\sin\theta & \cos\theta \end{bmatrix}. \tag{45}$$

θ in Eq. (45) is the angle between the fracture path and the horizontal axis. $\mathbf{\Lambda}$ is used here to transform the cohesive traction $\boldsymbol{t}$, formulated in the local coordinate system, to the global coordinate system.

The nonlinear system of Eqs. (42) needs to be solved iteratively. We adopt the Newton–Raphson resolution algorithm, in which Eqs. (42) are linearized with respect to displacements at the equilibrium iteration k of the incremental step $n + 1$, as follows:

$$\begin{bmatrix} \boldsymbol{R}^u \\ \boldsymbol{R}^a \end{bmatrix}_{n+1}^{k+1} = \begin{bmatrix} \boldsymbol{R}^u \\ \boldsymbol{R}^a \end{bmatrix}_{n+1}^{k} + \boldsymbol{J}_{n+1}^{k} \begin{bmatrix} \delta\boldsymbol{u} \\ \delta\boldsymbol{a} \end{bmatrix}_{n+1}^{k} = \boldsymbol{0} \tag{46}$$

where $\boldsymbol{J}$ is the Jacobian matrix (or the consistent tangent stiffness matrix), expressed as:

$$\boldsymbol{J} = \begin{bmatrix} \boldsymbol{R}^u_{,u} & \boldsymbol{R}^u_{,a} \\ \boldsymbol{R}^a_{,u} & \boldsymbol{R}^a_{,a} \end{bmatrix} = \begin{bmatrix} \boldsymbol{K}_{uu} & \boldsymbol{K}_{ua} \\ \boldsymbol{K}_{ua}^T & \boldsymbol{K}_{aa} + \boldsymbol{K}_{coh} \end{bmatrix} \tag{47}$$

in which $\boldsymbol{K}_{\alpha\beta}$ is the tangent stiffness matrix, expressed as

$$\boldsymbol{K}_{\alpha\beta} = \int_{\Omega} \left(\boldsymbol{B}_{\alpha}^T \mathbb{S}^{-1}(\Omega) \boldsymbol{B}_{\beta} + \boldsymbol{B}_{\alpha}^T \frac{\partial \mathbb{S}^{-1}}{\partial \boldsymbol{u}} \boldsymbol{B}_{\beta} \boldsymbol{u} \right) \mathrm{d}\Omega, \tag{48}$$

and $\boldsymbol{K}_{coh}$ is the cohesive stiffness $\boldsymbol{K}_{coh} = \partial \boldsymbol{F}^{\mathrm{coh}} / \partial \boldsymbol{a}$, which can be obtained explicitly through $\partial(T_n, T_t) / \partial(\Delta_n, \Delta_t)$. Note that in the FEM, the analytical expression of $\boldsymbol{J}$ is typically sought so as to achieve a quadratic convergence rate. Unfortunately, due to the particular formulation of the continuum damage model, we cannot obtain the analytical expression of the second term of Eq. (48) because the stiffness tensor $\mathbb{C} = \mathbb{S}^{-1}$ cannot be expressed explicitly. So we use the secant stiffness matrix method, in which only the first term of Eq. (48) is considered. Convergence can still be achieved at the cost of more iterations (linear convergence rate).

4.3. Fracture tip advancement algorithm

In order to couple the CZM and the nonlocal CDM model with the XFEM, an explicit algorithm is needed: (1) To determine when to split bulk elements and to insert a cohesive segment; (2) To calculate the propagation direction of the macro-fracture; and (3) To determine the fracture propagation length. In Section 3, we calibrated the transition from continuum damage to macro-fracture and we found that the critical damage value is $\Omega_{crit} = 0.2$ for the continuum damage model presented in Section 2. A simple implementation scheme consists in checking systematically the state variables at the Gauss points of elements ahead of fracture tip (Fig. 9). If the value of damage at one Gauss point exceeds Ω_{crit}, the fracture tip advances towards that Gauss point, with known propagation direction and length. However, this simple algorithm becomes ineffective when multiple Gauss points at different locations exceed the threshold at the same load increment. Let us recall that the continuum damage model is enhanced with nonlocal regularization for tensile softening, thus, the area of damage development ahead of the fracture tip (i.e. the size of process zone) is correlated with the internal length parameter l_c, as shown in Fig. 9. Like in the methods presented in [16,65], we assume that the fracture propagates when the component of the weighted damage tensor over the half circle patch ahead of the fracture tip (shaded in blue) exceeds the threshold Ω_{crit}. We first obtain the weighted damage tensor $\bar{\mathbf{\Omega}}$ using the bell-shaped weight function $\omega_0(\|\boldsymbol{x} - \boldsymbol{\xi}\|)$ through

$$\bar{\mathbf{\Omega}}(\boldsymbol{x}_{tip}) = \int_{\Omega_T} \omega(\boldsymbol{x}_{tip}, \boldsymbol{\xi}) \mathbf{\Omega}(\boldsymbol{\xi}) \mathrm{d}\Omega_T(\boldsymbol{\xi}) = \frac{\sum_{j=1}^{N_{GP}} \omega_0(\|\boldsymbol{x}_{tip} - \boldsymbol{\xi}_j\|) \mathbf{\Omega}(\boldsymbol{\xi}_j) \Delta V_j}{\sum_{j=1}^{N_{GP}} \omega_0(\|\boldsymbol{x}_{tip} - \boldsymbol{\xi}_j\|) \Delta V_j} \tag{49}$$

where $\boldsymbol{x}_{tip}$ and $\boldsymbol{\xi}$ are the global coordinates of fracture tip and Gauss points in Ω_T, respectively. N_{GP} is the total number of Gauss points in Ω_T, and ΔV_J is the geometrical volume associated with Gauss point j. Please note that the size of Ω_T is controlled by the internal length l_c since we chose a bell-shaped weight function (17) for nonlocal enhancement.

We discretize the half circle shown in Fig. 9 into a series of directions $\boldsymbol{m}$, and we project the weighted damage tensor on the direction $\boldsymbol{n}$ normal to the direction $\boldsymbol{m}$ used for discretization: $\Omega_n = \boldsymbol{n}^T \cdot \mathbf{\Omega} \cdot \boldsymbol{n}$. Then we compare the
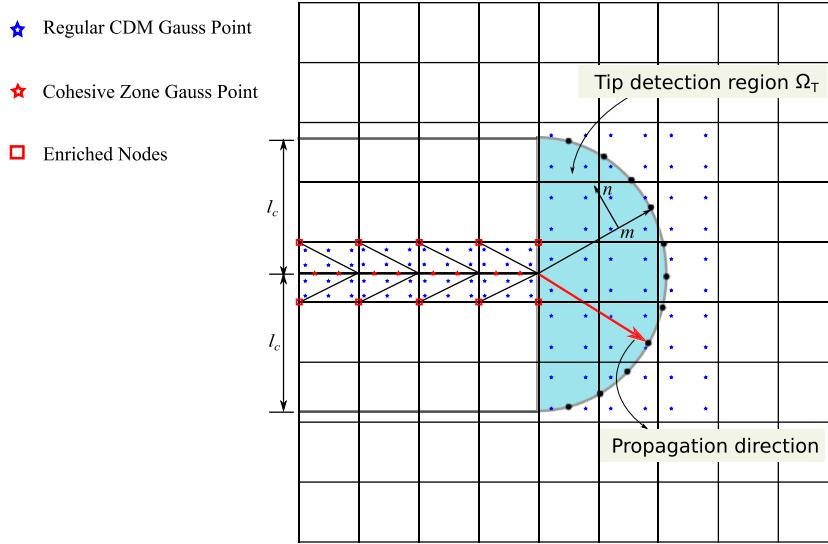
Fig. 9. Macro cohesive fracture initiation algorithm based on the projection of the weighted damage tensor.

maximum value of the projected damage components, $\max(\Omega_n)$, with the threshold Ω_{crit}. If $\max(\Omega_n) \geq \Omega_{crit}$, we propagate the fracture along the direction of m normal to the unit vector n. For all the simulations in this paper, we choose a user-defined growth length $\Delta a = l_c$, since the size of the process zone is controlled by the internal length and equal to $2 \times l_c$. It is worth noting that a cohesive segment is not inserted into an element unless the element is completely cut by the fracture (see Fig. 9). At all times, the balance of energy is ensured because the energy that would be dissipated by a small segment of discrete fracture is actually dissipated in the form of continuum damage.

4.4. SPR state variable mapping

An element being cut by a fracture should be divided into subdomains inside which the displacements are continuous functions. In this study, we employ the classical sub-region quadrature technique [66] to divide a quadrilateral element into multiple triangles, and we use three Gauss points within each triangle to calculate the Jacobian matrix and the residual. Consequently, the number and the location of Gauss points with in an element that is cut during fracture propagation is changed. It is thus necessary to remap the internal and state variables, such as damage and stress, from the initial to the new set of Gauss points. Variable mapping accuracy has a significant influence on the equilibrium recovery rate after the fracture tip advancement. In this paper, the super-convergent patch recovery (SPR) proposed by Zienkiewicz and Zhu [67] is adopted. In the SPR, two steps need to be performed numerically: (1) A construction step, in which the state variables at nodes of an element are interpolated by least square fitting from the neighboring Gauss points; (2) A recovery step, in which the state variables at the new Gauss points are interpolated from the nodes by using the shape functions of the element.

5. Engineering examples of micro–macro fracture propagation

5.1. Wedge splitting

We implemented the coupled CDM–CZM framework based on the XFEM into an open source finite element package programmed in C++, called 'Object-Oriented Finite Element Method' (OOFEM) [68,69]. To check that the framework can be used to model micro–macro fracture propagation, a wedge splitting benchmark example is first simulated. The geometry and boundary conditions are shown in Fig. 10. The thickness of the specimen is 97 mm, like in the laboratory experiment described in [70]. The material parameters listed in Table 1 are used, in which the elastic constants (E_0, ν_0) and the total energy release rate G_f are adopted from [70]. Note that l_c is typically
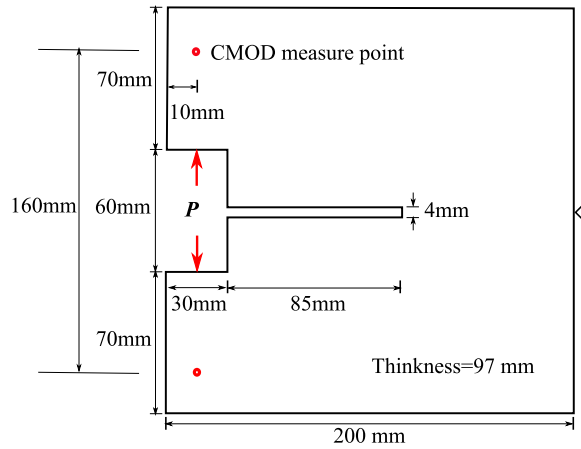
Fig. 10. Geometry and boundary conditions of the wedge splitting test.

Table 1
Material parameters used for the wedge splitting test.

Young's modulus	E_0 (GPa)	25.2
Poisson's ratio	ν_0	0.2
Damage evolution parameters	η	1.325×10^{-4}
	κ	2.5×10^{-4}
Internal length	l_c (mm)	16
Total energy release rate	G_f (N/mm)	0.101

2–3 times the maximum aggregate size in brittle solids [49]. We calibrate the damage evolution parameters (η, κ) for an internal length of $l_c = 16$ mm, by matching the numerical load–displacement curve to the experimental one. The domain is discretized with linear quadrilateral elements with two different mesh densities to investigate mesh dependency. It is expected that a horizontal fracture will initiate from the notch and will gradually propagate into a horizontal fracture in pure mode I.

As shown in Fig. 11, we simulate wedge-splitting test with different values of (η, κ) until the simulated force-CMOD (crack mouth opening displacement) curves (dashed lines) match well the experimental measurements [70] (solid dark line). In addition, we simulate a case in which the matrix is elastic (no damage) and in which the energy is solely dissipated by macro fracture surface formation (CZM). For this particular case, we used a cohesive strength of 6.6 MPa from [70], and the cohesive segments along the pre-assigned fracture path were inserted at the start of simulation. The global force-CMOD response of the CZM is represented by a solid blue line in Fig. 11. The curves predicted by the proposed CDM–CZM framework match the experimental data until the maximum force is reached. After the peak, the CDM–CZM simulation results are similar to those obtained with the CZM, but depart from the experimental response by up to 25%. These discrepancies can be explained by: (i) The zero-thickness of the pre-assigned cohesive segment, which has artificial compliance; this results in additional CMOD in the CZM simulation before the peak; (ii) The shape of the cohesive traction–separation law, which influences the global softening curve: the shape factors $\alpha = \beta = 4$ used in the PPR cohesive law are not appropriate for this particular material: Note that $\alpha/\beta < 2$ results in convex softening for ductile materials, $\alpha/\beta > 2$ results in concave softening for brittle/quasi-brittle material. Sophisticated calibration methods will be developed for the shape factors in future work. Overall, the global response reflected in the load–CMOD curve is predicted accurately before the peak; an error of up to 25% is made between the peak and a residual load of 1 kN, and the error is around 65% when the residual load is close to zero.

Fig. 12 shows several stages of the macro fracture propagation accompanied by damage process zone evolution. The tip of the macro cohesive fracture is behind the front of the process zone at all stages, which indicates a smooth transition from damage to fracture. The size of the process zone is constant throughout the simulation, and, due to nonlocal enhancement, the response is not mesh-dependent. Note that the maximum damage within the process
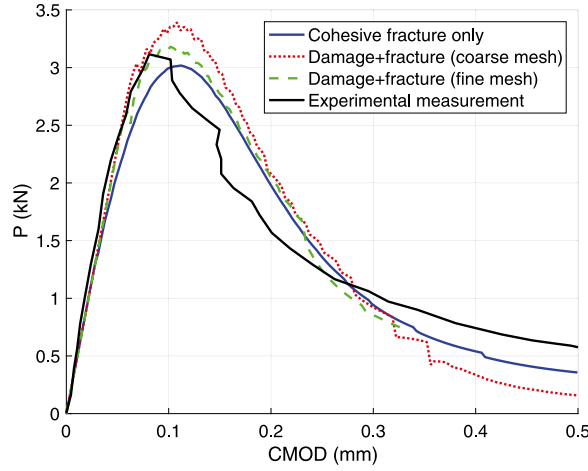
Fig. 11. Load vs. CMOD response: comparison of numerical and experimental results. (For interpretation of the references to color in this figure legend, the reader is referred to the web version of this article.)
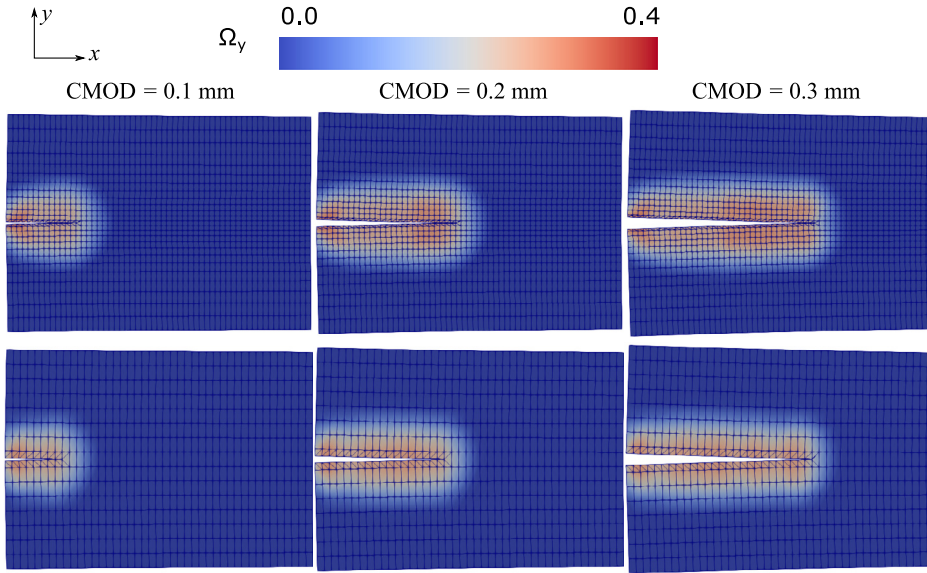

Fig. 12. Contour of the damage component Ω_y (horizontal micro cracks) and macro cohesive fracture path shown on the deformed mesh (displacements magnified ×5). Top row: fine mesh with 1450 elements in the zone of interest; lower row: coarse mesh with 645 elements in the zone of interest.

zone is $\max(\Omega_y) = 0.4$ - greater than the damage threshold $\Omega_{crit} = 0.2$. This is due to the fact that the threshold Ω_{crit} is applied on a weighted damage tensor and not on the components of damage itself.

Fig. 13 illustrates the transformation of the energy input into elastic deformation energy and dissipated energy over time, as a function of the CMOD. E_T denotes the total energy input, computed by multiplying the applied force P with the displacement at the nodes where the force is applied. E_E is the elastic energy stored within the system. E_C represents the dissipated cohesive energy due to macro fracture propagation, and it is calculated by multiplying the cohesive energy release rate ϕ_n by the length of propagated macro fracture, and the thickness of the specimen. The last term E_Ω is the dissipated energy due to micro fracture development; it can be computed by Eq. (33). We present the evolution of energy for the three cases simulated in Fig. 11 (CZM only, CDM–CZM with a coarse mesh, CDM–CZM with a fine mesh). Similar to the load–displacement curve, the differences between the three cases are due to the artificial compliance of the CZM and to the shape factors of the PPR cohesive model. Despite these
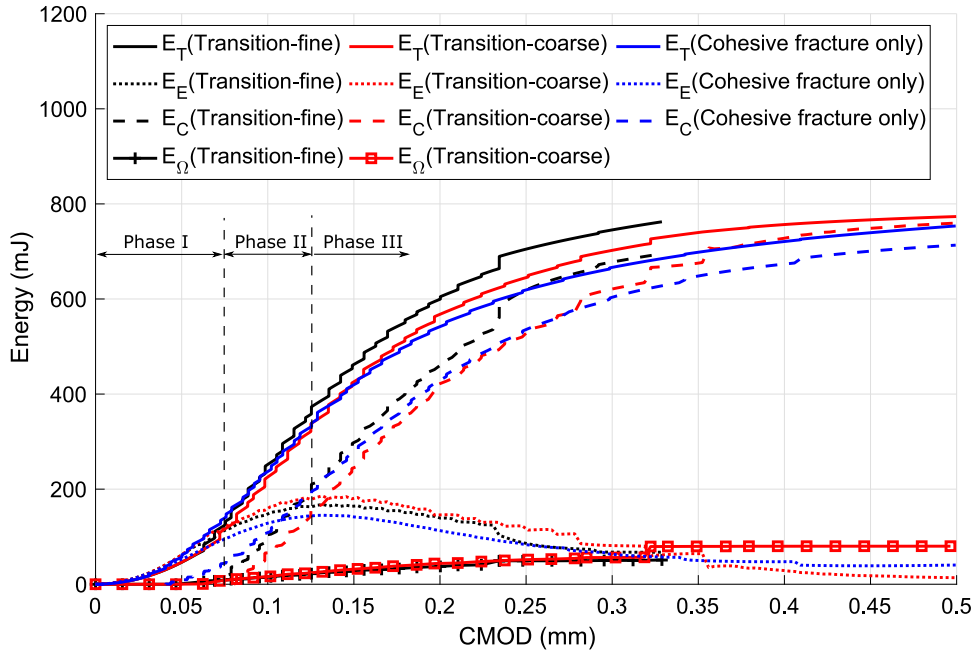
Fig. 13. Evolution of the components of energy during the wedge splitting test: work input E_T, elastic energy E_E, dissipated energy by cohesive fracture propagation E_C and by continuum damage E_Ω. CZM only ("Cohesive fracture only"), CDM–CZM with coarse mesh ("Transition-coarse"), CDM–CZM with fine mesh ("Transition-fine").

discrepancies, all the simulated cases show that the evolution of energy follows three phases. In the initial phase, all the input work is transformed and stored as elastic energy within the system. In the second phase, energy is dissipated by micro-crack and macro-fracture propagation while the elastic energy of the system keeps increasing. In the final phase, most of the input work is dissipated immediately, and some of the stored elastic energy gets dissipated as well, to propagate the micro-cracks and the macro-fracture. The elastic energy of the system tends to zero. We can also note that the percentage of energy dissipated by micro-crack propagation (damage development) is significantly smaller than the amount of energy dissipated by macro-fracture surface formation. To conclude, the proposed framework can successfully simulate mode I macro-fracture propagation with a damage process zone, the size of which depends on microstructure properties. Most of the input work is dissipated to create macro-fracture surfaces.

5.2. Three-point bending

A three-point bending test is simulated with the proposed nonlocal CDM–CZM model. The geometry and boundary conditions of the laboratory experiment described in [71] are adopted here — see Fig. 14. An initial notch of 20 mm in depth and 4 mm in width is considered. The thickness of the specimen is 100 mm. Like in the previous case, the elastic constants and the total energy release rate measured from [71] are directly used for the simulation. The internal length is fixed as $l_c = 12$ mm, and the material parameters controlling continuum damage evolution are calibrated by fitting the force–deflection curve against experimental results. We used two mesh densities. Both mesh densities yielded the same results (Fig. 15), which demonstrates that nonlocal regularization can alleviate mesh dependency. We adjusted the material parameters by trial and error; the best match was found to be the one shown in Fig. 15, in which the experimental data is represented by a black solid curve, and the numerical prediction is marked in dashed lines.

We also simulated the three-point bending test with CZM only by inserting cohesive segments aligned with the notch before the loading simulation, using the coarser mesh density. The CZM global response curve ($F - u$) marked in blue solid line matches the results obtained with the CDM–CZM framework. Note that for the case with
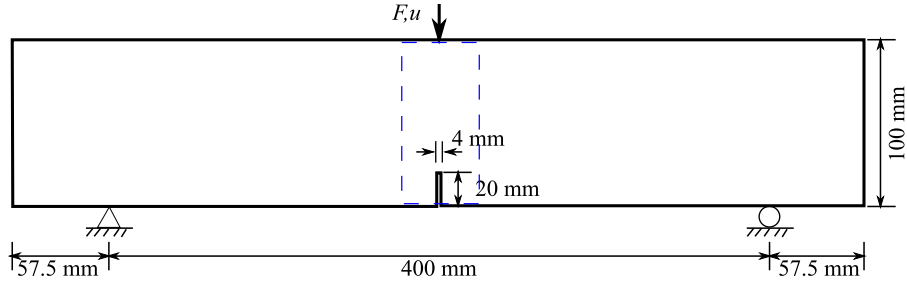
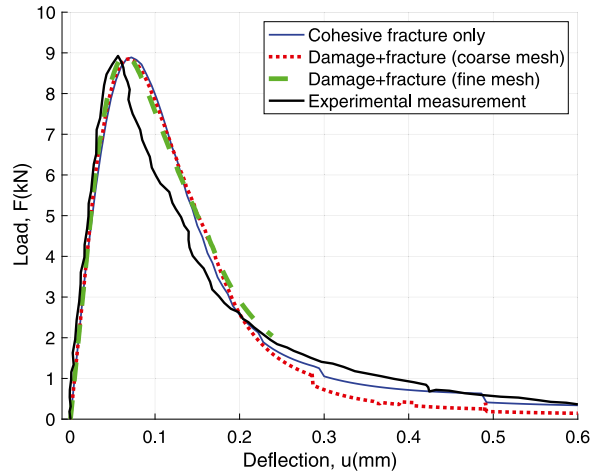**Fig. 14.** Geometry and boundary conditions of the three-point bending test.

Fig. 15. Load–deflection curve for the three-point bending test: comparison of experimental and numerical results.

Table 2

Material parameters used for the three-point bending test.

Young's modulus	E_0 (GPa)	50.0
Poission's ratio	ν_0	0.2
Damage evolution parameters	η	8.5×10^{-5}
	κ	3.0×10^{-4}
Internal length	l_c (mm)	12
Total energy release rate	G_f (N/mm)	0.1963

CZM only, we chose the cohesive strength $\sigma_{\max} = 6.12$ MPa and the cohesive energy release rate $\phi_n = G_f = 0.1963$ N/mm, from [71]. The 6 CDM–CZM parameters used for the simulations are listed in Table 2.

Fig. 16 represents the distribution of horizontal stress σ_x, nonlocal equivalent strain $\hat{\epsilon}^{nl}$ and damage component Ω_x obtained with the coarser mesh in the central zone of the beam, marked by a blue dashed in Fig. 14. The traction–separation law predicts traction (reflected from σ_x) even after the initiation of the macro-fracture. The material fracture tip (no traction, defined in Fig. 5) is behind the mathematical fracture tip (cohesive segment inserted). The nonlocal equivalent strain is non-zero only in the vicinity of the macro fracture tip area, indicating that the fracture surface behind the material fracture tip is unloaded: the elastic energy stored during previous load increments flows into the tip area and is dissipated. Vertical micro-cracks develop within the process zone, which surrounds the macro-fracture.

Fig. 17 shows the evolution of the total input work E_T, the stored elastic energy E_E, and the dissipated energy by macro cohesive fracture propagation E_C and by micro-cracks development E_Ω. Similar to the wedge splitting case, the evolution of energy presents three main phases, and the percentage of dissipated energy by micro-crack initiation and propagation E_Ω is insignificant compared to the energy dissipated by macro-fracture formation. It is also worth
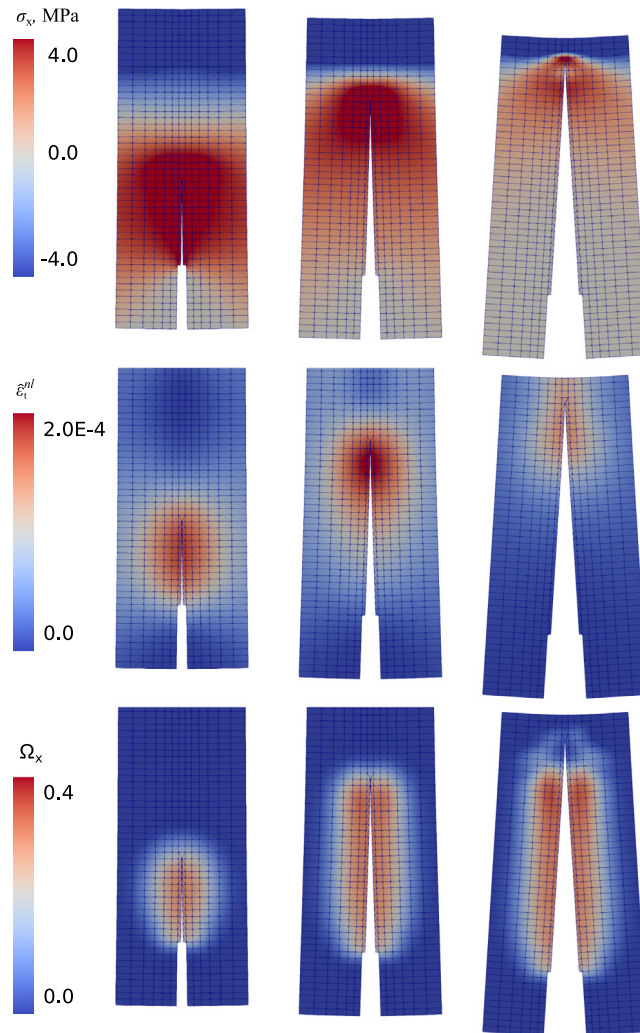
Fig. 16. Contour of horizontal stress σ_x, nonlocal equivalent strain $\hat{\varepsilon}_t^{nl}$ and damage component Ω_x (vertical micro cracks) in the central part of the beam subjected to three-point bending (see blue area in Fig. 14). Deformed mesh ($\times 50$) at different stages of macro fracture propagation.

noting that a discrepancy exists between the predictions made by the proposed CDM–CZM framework and those made by the CZM alone, even if the global responses ($F - u$ curve in Fig. 15) are similar. This result indicates that the technique of pre-inserting cohesive elements along the fracture path (CZM alone) leads to an inaccurate energy dissipation, due to artificial stiffness. Dynamically inserting cohesive elements (CDM–CZM framework) is more accurate in terms of energy dissipation.

6. Conclusions

In this paper, we present a novel numerical framework that couples a nonlocal micromechanics based anisotropic damage model with a cohesive zone model. This multi-scale framework captures the failure process in brittle solids, from the nucleation of micro-cracks to the formation of macro-fracture.

A nonlocal micromechanics-based continuum damage model is proposed to predict the material response from the microscopic scale to the REV scale. A dilute homogenization scheme is adopted for calculating the deformation energy of the REV, which is attributed to the elastic deformation of the matrix and to the displacement jumps at open and closed micro-crack faces. The Gibbs free energy is obtained by integrating the energy potentials of the
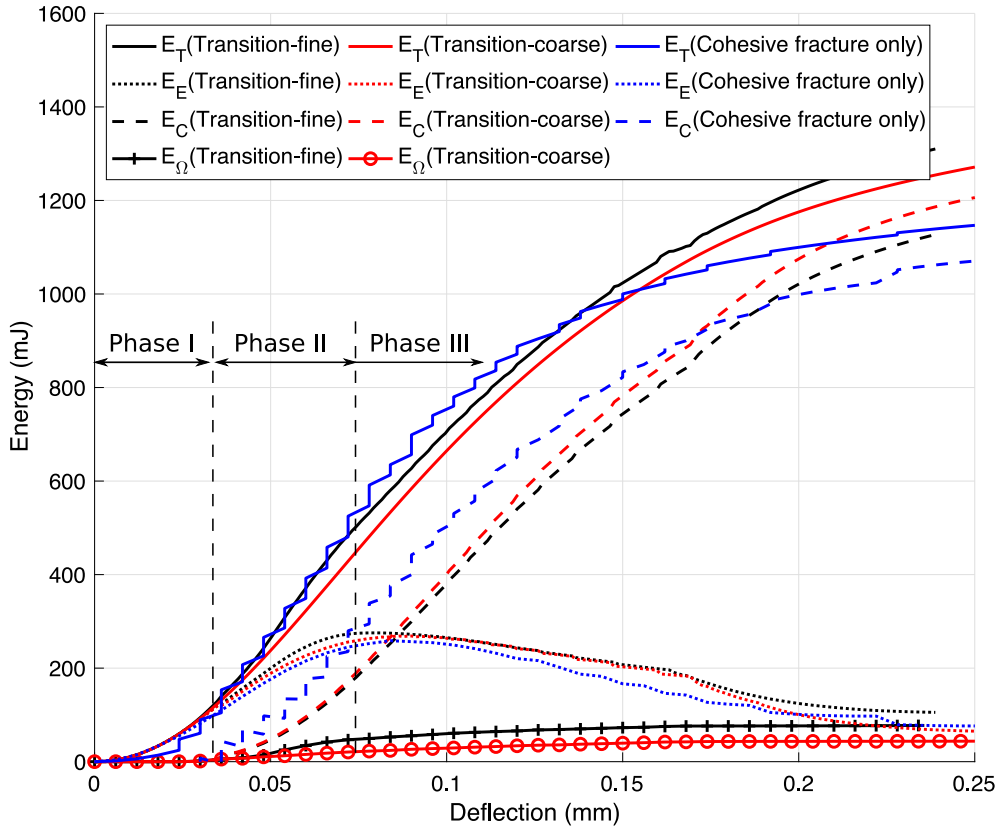
Fig. 17. Evolution of the components of energy during the three-point bending test: work input E_T, elastic energy E_E, dissipated energy by cohesive fracture propagation E_C and by continuum damage E_Ω. CZM only ("Cohesive fracture only"), CDM–CZM with coarse mesh ("Transition-coarse"), CDM–CZM with fine mesh ("Transition-fine").

different sets of micro-cracks on the unit sphere. An explicit expression of the free energy of the REV is provided when all micro-cracks are open and when all micro-cracks are closed. Tensile damage criteria depend on equivalent strains defined in terms of positive principal strains. Damage evolution law is obtained from consistency condition and from postulate on damage potential. The model is enriched by nonlocal equivalent strain, calculated as the weighted average of equivalent strain on an influence zone of material-specific characteristic size.

From the REV scale to the macroscopic scale, the potential based PPR cohesive zone model is adopted to characterize the macro-fracture behavior. The critical damage level that marks the transition from continuum damage to discrete cohesive fracture is defined as the damage above which the damage stiffness tensor calculated with the proposed nonlocal damage model (which does not account for crack interactions) stops matching the stiffness tensor calculated from Kachanov's micromechanics-based damage model (which accounts for crack interactions). We find a critical damage threshold of 0.2. Furthermore, an energy equivalence criterion is established to determine the cohesive strength and the cohesive energy release rate, so that the total dissipated energy by propagating macro-fracture and micro-cracks for a unit area equals the energy release rate measured in the laboratory.

We couple the nonlocal continuum damage model with the discrete cohesive zone model by using a XFEM discretization technique. After deriving the secant Jacobian matrix, we implement the proposed framework into an open source finite element package. A weighted damage tensor around the tip area is employed to determine the direction and length of the macro-fracture that propagates. The SPR method is used to map state variables after remeshing. Utilizing the proposed computational tool, a wedge splitting test and a three-point bending test are simulated. Results demonstrate that the framework can successfully capture the propagation of a mode I macro-fracture within a damage process zone. The size of the process zone is mesh independent owing to the nonlocal regularization, and the predicted global responses match satisfactorily the experimental measurements. In addition,

simulation results reveal that most of the energy is dissipated to create macro-fracture surfaces and that the amount of energy dissipated by damage development is negligible.

The proposed CDM–CZM framework still have limitations. For instance, it is impossible to properly simulate micro–macro fracture propagation in mixed mode, due to the choice of the constitutive CDM model. First, it is impossible to obtain the tangent Jacobian matrix without the explicit expression of the damage stiffness matrix **C**, which results in convergence issues for complex stress paths. Second, the dilute homogenization scheme limits the degradation of modulus, so that the softening stress–strain curve cannot reach zero stress, which can weaken the performance of nonlocal regularization. This challenge will be addressed in future studies by employing the Mori-Tanaka homogenization scheme, which accounts for crack interaction.

Acknowledgments

Appendix. Derivation of the free enthalpy

The derivation of the expression of the free enthalpy (Eq. (6)) is obtained by integrating the free enthalpy of single family cracks (Eq. (1)) over the unit sphere and by using the definition of damage tensor in Eq. (5). Since there are 2 terms in the kernel of the integral, we show them one by one in the following for the case of open cracks:

$$
\begin{aligned}
&\frac{1}{8\pi} \int_{S^2} \{c_0\, \rho(\overrightarrow{n})(\overrightarrow{n}\cdot\boldsymbol{\sigma}\cdot\overrightarrow{n})\langle\overrightarrow{n}\cdot\boldsymbol{\sigma}\cdot\overrightarrow{n}\rangle^{+}\}\mathrm{d}S \\
&= \frac{3c_0}{16\pi} \int_{S^2} (5\overrightarrow{n}\cdot\boldsymbol{\Omega}\cdot\overrightarrow{n} - \mathrm{Tr}\boldsymbol{\Omega})(\overrightarrow{n}\cdot\boldsymbol{\sigma}\cdot\overrightarrow{n})^2\mathrm{d}S
\end{aligned}
\tag{50}
$$

in which

$$
\begin{aligned}
&5\int_{S^2} (\overrightarrow{n}\cdot\boldsymbol{\Omega}\cdot\overrightarrow{n})(\overrightarrow{n}\cdot\boldsymbol{\sigma}\cdot\overrightarrow{n})^2\mathrm{d}S \\
&= 5(\boldsymbol{\Omega}\otimes\boldsymbol{\sigma}) :: \int_{S^2} \overrightarrow{n}\otimes\overrightarrow{n}\otimes\overrightarrow{n}\otimes\overrightarrow{n}\otimes\overrightarrow{n}\otimes\overrightarrow{n}\,\mathrm{d}S : \boldsymbol{\sigma} \\
&= \frac{4\pi}{21}\mathrm{Tr}\boldsymbol{\Omega}(\mathrm{Tr}\boldsymbol{\sigma})^2 + \frac{32\pi}{21}\mathrm{Tr}(\boldsymbol{\sigma}\cdot\boldsymbol{\sigma}\cdot\boldsymbol{\Omega}) + \frac{16\pi}{21}\mathrm{Tr}\boldsymbol{\sigma}\,\mathrm{Tr}(\boldsymbol{\Omega}\cdot\boldsymbol{\sigma}) + \frac{8\pi}{21}\mathrm{Tr}\boldsymbol{\Omega}\,\mathrm{Tr}(\boldsymbol{\sigma}\cdot\boldsymbol{\sigma}),
\end{aligned}
\tag{51}
$$

and

$$
-\mathrm{Tr}\boldsymbol{\Omega} \int_{S^2} (\overrightarrow{n}\cdot\boldsymbol{\sigma}\cdot\overrightarrow{n})^2\mathrm{d}S = \frac{-4\pi}{15}\mathrm{Tr}\boldsymbol{\Omega}(\mathrm{Tr}\boldsymbol{\sigma})^2 + \frac{-8\pi}{15}\mathrm{Tr}\boldsymbol{\Omega}\,\mathrm{Tr}(\boldsymbol{\sigma}\cdot\boldsymbol{\sigma}).
\tag{52}
$$

Similarly, we have

$$
\begin{aligned}
&\frac{1}{8\pi} \int_{S^2} \{c_1\rho(\overrightarrow{n})[(\boldsymbol{\sigma}\cdot\boldsymbol{\sigma}):(\overrightarrow{n}\otimes\overrightarrow{n}) - \boldsymbol{\sigma}:(\overrightarrow{n}\otimes\overrightarrow{n}\otimes\overrightarrow{n}\otimes\overrightarrow{n}):\boldsymbol{\sigma}]\}\mathrm{d}S \\
&= \frac{3c_1}{16\pi} \int_{S^2} \{(5\overrightarrow{n}\cdot\boldsymbol{\Omega}\cdot\overrightarrow{n} - \mathrm{Tr}\boldsymbol{\Omega})[(\boldsymbol{\sigma}\cdot\boldsymbol{\sigma}):(\overrightarrow{n}\otimes\overrightarrow{n}) - \boldsymbol{\sigma}:(\overrightarrow{n}\otimes\overrightarrow{n}\otimes\overrightarrow{n}\otimes\overrightarrow{n}):\boldsymbol{\sigma}]\}\mathrm{d}S
\end{aligned}
\tag{53}
$$

where

$$
5\int_{S^2} \{(\overrightarrow{n}\cdot\boldsymbol{\Omega}\cdot\overrightarrow{n})\otimes(\boldsymbol{\sigma}\cdot\boldsymbol{\sigma}):(\overrightarrow{n}\otimes\overrightarrow{n})\}\mathrm{d}S = \frac{8\pi}{3}\mathrm{Tr}(\boldsymbol{\sigma}\cdot\boldsymbol{\sigma}\cdot\boldsymbol{\Omega}) + \frac{4\pi}{3}\mathrm{Tr}\boldsymbol{\Omega}\,\mathrm{Tr}(\boldsymbol{\sigma}\cdot\boldsymbol{\sigma}),
\tag{54}
$$

$$
-\mathrm{Tr}\boldsymbol{\Omega} \int_{S^2} (\boldsymbol{\sigma}\cdot\boldsymbol{\sigma}):(\overrightarrow{n}\otimes\overrightarrow{n})\mathrm{d}S = \frac{-4\pi}{3}\mathrm{Tr}\boldsymbol{\Omega}\,\mathrm{Tr}(\boldsymbol{\sigma}\cdot\boldsymbol{\sigma}),
\tag{55}
$$

$$
-\mathrm{Tr}\boldsymbol{\Omega} \int_{S^2} -\boldsymbol{\sigma}:(\overrightarrow{n}\otimes\overrightarrow{n}\otimes\overrightarrow{n}\otimes\overrightarrow{n}):\boldsymbol{\sigma}\,\mathrm{d}S = \frac{4\pi}{15}\mathrm{Tr}\boldsymbol{\Omega}(\mathrm{Tr}\boldsymbol{\sigma})^2 + \frac{8\pi}{15}\mathrm{Tr}\boldsymbol{\Omega}\,\mathrm{Tr}(\boldsymbol{\sigma}\cdot\boldsymbol{\sigma}).
\tag{56}
$$

After summing up all the coefficients, we can obtain the portion of the macroscopic free enthalpy that is due to the micro-cracks in terms of the second order damage tensor $\boldsymbol{\Omega}$, as follows:

$$
\begin{aligned}
G^{crack} =& \frac{v_0}{140} c_1 \operatorname{Tr}\boldsymbol{\Omega}(\operatorname{Tr}\boldsymbol{\sigma})^2 + \frac{7 - 2v_0}{14} c_1 \operatorname{Tr}(\boldsymbol{\sigma} \cdot \boldsymbol{\sigma} \cdot \boldsymbol{\Omega}) \\
&+ \frac{-v_0}{14} c_1 \operatorname{Tr}\boldsymbol{\sigma} \operatorname{Tr}(\boldsymbol{\Omega} \cdot \boldsymbol{\sigma}) + \frac{v_0}{70} c_1 \operatorname{Tr}\boldsymbol{\Omega} \operatorname{Tr}(\boldsymbol{\sigma} \cdot \boldsymbol{\sigma})
\end{aligned}
\tag{57}
$$

Note that the relations $(\overrightarrow{n} \cdot \boldsymbol{\sigma} \cdot \overrightarrow{n})^2 = \boldsymbol{\sigma} : (\overrightarrow{n} \otimes \overrightarrow{n} \otimes \overrightarrow{n} \otimes \overrightarrow{n}) : \boldsymbol{\sigma}$ and $c_0 = \frac{2 - v_0}{2} c_1$ are used for the derivation. The energy expression for closed micro-cracks will have no contribution from Eq. (50) since $\langle \overrightarrow{n} \cdot \boldsymbol{\sigma} \cdot \overrightarrow{n} \rangle^+ = 0$, and it is reflected by the different set of coefficients in Eq. (6).

References

[1] Y. Ma, H. Huang, Dem analysis of failure mechanisms in the intact brazilian test, Int. J. Rock Mech. Min. Sci. 102 (2018) 109–119.
[2] A. Yin, X. Yang, S. Yang, W. Jiang, Multiscale fracture simulation of three-point bending asphalt mixture beam considering material heterogeneity, Eng. Fract. Mech. 78 (12) (2011) 2414–2428.
[3] J. Oliver, M. Caicedo, E. Roubin, A.E. Huespe, J.A. Hernández, Continuum approach to computational multiscale modeling of propagating fracture, Comput. Methods Appl. Mech. Engrg. 294 (2015) 384–427.
[4] M.G. Geers, V.G. Kouznetsova, W. Brekelmans, Multi-scale computational homogenization: Trends and challenges, J. Comput. Appl. Math. 234 (7) (2010) 2175–2182.
[5] F. Feyel, A multilevel finite element method (fe2) to describe the response of highly non-linear structures using generalized continua, Comput. Methods Appl. Mech. Eng. 192 (28–30) (2003) 3233–3244.
[6] T. Massart, R. Peerlings, M. Geers, An enhanced multi-scale approach for masonry wall computations with localization of damage, Internat. J. Numer. Methods Engrg. 69 (5) (2007) 1022–1059.
[7] T. Belytschko, S. Loehnert, J.H. Song, Multiscale aggregating discontinuities: a method for circumventing loss of material stability, Internat. J. Numer. Methods Engrg. 73 (6) (2008) 869–894.
[8] T. Belytschko, J.H. Song, Coarse-graining of multiscale crack propagation, Internat. J. Numer. Methods Engrg. 81 (5) (2010) 537–563.
[9] M. Kulkarni, K. Matouš, P. Geubelle, Coupled multi-scale cohesive modeling of failure in heterogeneous adhesives, Internat. J. Numer. Methods Engrg. 84 (8) (2010) 916–946.
[10] C.V. Verhoosel, J.J. Remmers, M.A. Gutiérrez, R. De Borst, Computational homogenization for adhesive and cohesive failure in quasi-brittle solids, Internat. J. Numer. Methods Engrg. 83 (8–9) (2010) 1155–1179.
[11] V.P. Nguyen, M. Stroeven, L.J. Sluys, An enhanced continuous–discontinuous multiscale method for modeling mode-i cohesive failure in random heterogeneous quasi-brittle materials, Eng. Fract. Mech. 79 (2012) 78–102.
[12] M. Jirasek, T. Zimmermann, Embedded crack model. part ii: Combination with smeared cracks, Internat. J. Numer. Methods Engrg. 50 (6) (2001) 1291–1305.
[13] A. Simone, G.N. Wells, L.J. Sluys, From continuous to discontinuous failure in a gradient-enhanced continuum damage model, Comput. Methods Appl. Mech. Engrg. 192 (41) (2003) 4581–4607.
[14] C. Comi, S. Mariani, U. Perego, An extended fe strategy for transition from continuum damage to mode i cohesive crack propagation, Int. J. Numer. Anal. Methods Geomech. 31 (2) (2007) 213.
[15] S. Cuvilliez, F. Feyel, E. Lorentz, S. Michel-Ponnelle, A finite element approach coupling a continuous gradient damage model and a cohesive zone model within the framework of quasi-brittle failure, Comput. Methods Appl. Mech. Engrg. 237 (2012) 244–259.
[16] Y. Wang, H. Waisman, From diffuse damage to sharp cohesive cracks: A coupled xfem framework for failure analysis of quasi-brittle materials, Comput. Methods Appl. Mech. Engrg. 299 (2016) 57–89.
[17] R. Peerlings, R. De Borst, J. De Vree, Gradient enhanced damage for quasi-brittle materials, Int. J. Numer. Methods Eng. 39 (De Vree, JHP) (1996) 3391–3403.
[18] J. De Vree, W. Brekelmans, M. Van Gils, Comparison of nonlocal approaches in continuum damage mechanics, Comput. Struct. 55 (4) (1995) 581–588.
[19] W. Jin, C. Arson, Anisotropic nonlocal damage model for materials with intrinsic transverse isotropy, Int. J. Solids Struct. 139 (2018) 29–42.
[20] M. Geers, R. De Borst, W. Brekelmans, R. Peerlings, Strain-based transient-gradient damage model for failure analyses, Comput. Methods Appl. Mech. Engrg. 160 (1) (1998) 133–153.
[21] A. Simone, H. Askes, L.J. Sluys, Incorrect initiation and propagation of failure in non-local and gradient-enhanced media, Int. J. Solids Struct. 41 (2) (2004) 351–363.
[22] S. Leon, D. Spring, G. Paulino, Reduction in mesh bias for dynamic fracture using adaptive splitting of polygonal finite elements, Internat. J. Numer. Methods Engrg. 100 (8) (2014) 555–576.
[23] C.V. Verhoosel, R. de Borst, A phase-field model for cohesive fracture, Internat. J. Numer. Methods Engrg. 96 (1) (2013) 43–62.
[24] G.Z. Voyiadjis, N. Mozaffari, Nonlocal damage model using the phase field method: theory and applications, Int. J. Solids Struct. 50 (20) (2013) 3136–3151.
[25] M. Ambati, T. Gerasimov, L. De Lorenzis, A review on phase-field models of brittle fracture and a new fast hybrid formulation, Comput. Mech. 55 (2) (2015) 383–405.

[26] J. Planas, M. Elices, G.V. Guinea, Cohesive cracks versus nonlocal models: Closing the gap, Int. J. Fract. 63 (2) (1993) 173–187.

[27] J. Mazars, G. Pijaudier-Cabot, From damage to fracture mechanics and conversely: a combined approach, Int. J. Solids Struct. 33 (20) (1996) 3327–3342.

[28] F. Cazes, M. Coret, A. Combescure, A. Gravouil, A thermodynamic method for the construction of a cohesive law from a nonlocal damage model, Int. J. Solids Struct. 46 (6) (2009) 1476–1490.

[29] F. Cazes, A. Simatos, M. Coret, A. Combescure, A cohesive zone model which is energetically equivalent to a gradient-enhanced coupled damage-plasticity model, Eur. J. Mech. A Solids 29 (6) (2010) 976–989.

[30] M. Jirasek, T. Zimmermann, Embedded crack model: I. basic formulation, Internat. J. Numer. Methods Engrg. 50 (6) (2001) 1269–1290.

[31] S.-N. Roth, P. Léger, A. Soulaïmani, A combined xfem–damage mechanics approach for concrete crack propagation, Comput. Methods Appl. Mech. Engrg. 283 (2015) 923–955.

[32] C. Comi, S. Mariani, U. Perego, From localized damage to discrete cohesive crack propagation in nonlocal continua, in: Proceedings of the Fifth World Congress on Computational Mechanics (WCCM V), Vienna University of Technology, 2002.

[33] Y. Wang, H. Waisman, Progressive delamination analysis of composite materials using xfem and a discrete damage zone model, Comput. Mech. 55 (1) (2015) 1–26.

[34] J. Leclerc, L. Wu, V.D. Nguyen, L. Noels, A damage to crack transition model accounting for stress triaxiality formulated in a hybrid nonlocal implicit discontinuous galerkin-cohesive band model framework, Internat. J. Numer. Methods Engrg. 113 (3) (2018) 374–410.

[35] K. Park, G.H. Paulino, J.R. Roesler, A unified potential-based cohesive model of mixed-mode fracture, J. Mech. Phys. Solids 57 (6) (2009) 891–908.

[36] J. Shao, D. Hoxha, M. Bart, F. Homand, G. Duveau, M. Souley, N. Hoteit, Modelling of induced anisotropic damage in granites, Int. J. Rock Mech. Min. Sci. 36 (8) (1999) 1001–1012.

[37] Q. Yang, W. Zhou, G. Swoboda, Micromechanical identification of anisotropic damage evolution laws, Int. J. Fract. 98 (1) (1999) 55–76.

[38] W. Jin, C. Arson, Nonlocal enrichment of a micromechanical damage model with tensile softening: Advantages and limitations, Comput. Geotech. 94 (2018) 196–206.

[39] W. Jin, C. Arson, Discrete equivalent wing crack based damage model for brittle solids, Int. J. Solids Struct. 110–111 (2017) 279–293.

[40] W. Jin, C. Arson, Micromechanics based discrete damage model with multiple non-smooth yield surfaces: theoretical formulation, numerical implementation and engineering applications, Int. J. Damage Mech. 27 (5) (2018) 611–639.

[41] V. Lubarda, D. Krajcinovic, Damage tensors and the crack density distribution, Int. J. Solids Struct. 30 (20) (1993) 2859–2877.

[42] M.L. Kachanov, Continuum model of medium with cracks, J. Eng. Mech. Div. 106 (5) (1980) 1039–1051.

[43] K. Hayakawa, S. Murakami, Thermodynamical modeling of elastic-plastic damage and experimental validation of damage potential, Int. J. Damage Mech. 6 (4) (1997) 333–363.

[44] J. Mazars, G. Pijaudier-Cabot, Continuum damage theory-application to concrete, J. Eng. Mech. 115 (2) (1989) 345–365.

[45] R. Peerlings, R. De Borst, W. Brekelmans, J. De Vree, I. Spee, Some observations on localisation in non-local and gradient damage models, Eur. J. Mech. A Solids 15 (1996) 937–954.

[46] F. Vernerey, W.K. Liu, B. Moran, Multi-scale micromorphic theory for hierarchical materials, J. Mech. Phys. Solids 55 (12) (2007) 2603–2651.

[47] C.G. Hoover, Z.P. Bažant, Cohesive crack, size effect, crack band and work-of-fracture models compared to comprehensive concrete fracture tests, Int. J. Fract. 187 (1) (2014) 133–143.

[48] G. Pijaudier-Cabot, Z.P. Bažant, Nonlocal damage theory, J. Eng. Mech. 113 (10) (1987) 1512–1533.

[49] Z.P. Bažant, G. Pijaudier-Cabot, Measurement of characteristic length of nonlocal continuum, J. Eng. Mech. 115 (4) (1989) 755–767.

[50] M.L. Kachanov, Elastic solids with many cracks: a simple method of analysis, Int. J. Solids Struct. 23 (1) (1987) 23–43.

[51] W. Jin, H. Xu, C. Arson, S. Busetti, Computational model coupling mode ii discrete fracture propagation with continuum damage zone evolution, Int. J. Numer. Anal. Methods Geomech. 41 (2017) 223–250.

[52] M.L. Kachanov, Effective elastic properties of cracked solids: critical review of some basic concepts, Appl. Mech. Rev. 45 (8) (1992) 304–335.

[53] L. Shen, S. Yi, New solutions for effective elastic moduli of microcracked solids, Int. J. Solids Struct. 37 (26) (2000) 3525–3534.

[54] L. Shen, J. Li, A numerical simulation for effective elastic moduli of plates with various distributions and sizes of cracks, Int. J. Solids Struct. 41 (26) (2004) 7471–7492.

[55] K. Park, H. Choi, G.H. Paulino, Assessment of cohesive traction-separation relationships in abaqus: A comparative study, Mech. Res. Commun. 78 (2016) 71–78.

[56] S.H. Song, G.H. Paulino, W.G. Buttlar, A bilinear cohesive zone model tailored for fracture of asphalt concrete considering viscoelastic bulk material, Eng. Fract. Mech. 73 (18) (2006) 2829–2848.

[57] K. Park, G.H. Paulino, Computational implementation of the ppr potential-based cohesive model in abaqus: educational perspective, Eng. Fract. Mech. 93 (2012) 239–262.

[58] K. Park, G.H. Paulino, Cohesive zone models: a critical review of traction-separation relationships across fracture surfaces, Appl. Mech. Rev. 64 (6) (2011) 060802.

[59] X. Xu, A. Needleman, Numerical simulations of fast crack growth in brittle solids, J. Mech. Phys. Solids 42 (9) (1994) 1397–1434.

[60] V.P. Nguyen, Discontinuous galerkin/extrinsic cohesive zone modeling: Implementation caveats and applications in computational fracture mechanics, Eng. Fract. Mech. 128 (2014) 37–68.

[61] W. Celes, G.H. Paulino, R. Espinha, A compact adjacency-based topological data structure for finite element mesh representation, Internat. J. Numer. Methods Engrg. 64 (11) (2005) 1529–1556.

[62] N. Moës, T. Belytschko, Extended finite element method for cohesive crack growth, Eng. Fract. Mech. 69 (7) (2002) 813–833.

[63] J.M. Melenk, I. Babuška, The partition of unity finite element method: basic theory and applications, Comput. Methods Appl. Mech. Engrg. 139 (1–4) (1996) 289–314.

[64] T.-P. Fries, A corrected xfem approximation without problems in blending elements, Internat. J. Numer. Methods Engrg. 75 (5) (2008) 503–532.

[65] G. Wells, L. Sluys, R. De Borst, Simulating the propagation of displacement discontinuities in a regularized strain-softening medium, Internat. J. Numer. Methods Engrg. 53 (5) (2002) 1235–1256.

[66] T.P. Fries, T. Belytschko, The extended/generalized finite element method: an overview of the method and its applications, Internat. J. Numer. Methods Engrg. 84 (3) (2010) 253–304.

[67] O.C. Zienkiewicz, J.Z. Zhu, The superconvergent patch recovery and a posteriori error estimates. part 1: The recovery technique, Internat. J. Numer. Methods Engrg. 33 (7) (1992) 1331–1364.

[68] B. Patzák, Z. Bittnar, Oofem–an object oriented framework for finite element analysis, Acta Polytech. 44 (5–6) (2004).

[69] B. Patzák, Oofem—an object-oriented simulation tool for advanced modeling of materials and structures, Acta Polytech. 52 (6) (2012).

[70] E. Denarie, V. Saouma, A. Iocco, D. Varelas, Concrete fracture process zone characterization with fiber optics, J. Eng. Mech. 127 (5) (2001) 494–502.

[71] D. Zhang, K. Wu, Fracture process zone of notched three-point-bending concrete beams, Cem. Concr. Res. 29 (12) (1999) 1887–1892.